From single-pulsed field gradient to double-pulsed field gradient MR: gleaning new microstructural information and developing new forms of contrast in MRI[†]

Noam Shemesh[a], Evren Özarslan[b], Michal E. Komlosh[b], Peter J. Basser[b] and Yoram Cohen[a]*

One of the hallmarks of diffusion NMR and MRI is its ability to utilize restricted diffusion to probe compartments much smaller than the excited volume or the MRI voxel, respectively, and to extract microstructural information from them. Single-pulsed field gradient (s-PFG) MR methodologies have been employed with great success to probe micro-structures in various disciplines, ranging from chemistry to neuroscience. However, s-PFG MR also suffers from inherent shortcomings, especially when specimens are characterized by orientation or size distributions: in such cases, the microstructural information available from s-PFG experiments is limited or lost. Double-pulsed field gradient (d-PFG) MR methodology, an extension of s-PFG MR, has attracted attention owing to recent theoretical studies predicting that it can overcome certain inherent limitations of s-PFG MR. In this review, we survey the microstructural features that can be obtained from conventional s-PFG methods in the different q regimes, and highlight its limitations. The experimental aspects of d-PFG methodology are then presented, together with an overview of its theoretical underpinnings and a general framework for relating the MR signal decay and material microstructure, affording new microstructural parameters. We then discuss recent studies that have validated the theory using phantoms in which the ground truth is well known *a priori*, a crucial step prior to the application of d-PFG methodology in neuronal tissue. The experimental findings are in excellent agreement with the theoretical predictions and reveal, *inter alia*, zero-crossings of the signal decay, robustness towards size distributions and angular dependences of the signal decay from which accurate microstructural parameters, such as compartment size and even shape, can be extracted. Finally, we show some initial findings in d-PFG MR imaging. This review lays the foundation for future studies, in which accurate and novel microstructural information could be extracted from complex biological specimens, eventually leading to new forms of contrast in MRI. Copyright © 2010 John Wiley & Sons, Ltd.

Keywords: double-PFG; microstructure; MRI; diffusion–diffraction; restricted diffusion; pore size; compartment shape; anisotropy

INTRODUCTION

The effect of diffusion on the NMR signal was observed as early as 1950 by Hahn (1). The potential of harnessing NMR as a methodology for measuring the diffusion coefficient of NMR-observable nuclei was recognized soon thereafter by Carr and Purcell (2), and the subsequent development of pulsed field gradient (PFG) NMR by Stejskal and Tanner (3) provided a feasible means for measuring the diffusion coefficient completely noninvasively and with great precision. Indeed, diffusion NMR has become the most important tool for characterizing diffusion in many scientific disciplines, ranging from chemistry to medicine.

Numerous comprehensive and authoritative reviews have been published on various diffusion MR methodologies and

* Correspondence to: Y. Cohen, School of Chemistry, The Raymond and Beverly Sackler Faculty of Exact Sciences, Tel Aviv University, Ramat Aviv, Tel Aviv 69978, Israel.

a N. Shemesh, Y. Cohen
School of Chemistry, The Raymond and Beverly Sackler Faculty of Exact Sciences, Tel Aviv University, Tel Aviv, Israel

b E. Özarslan, M. E. Komlosh, P. J. Basser
Section on Tissue Biophysics and Biomimetics, NICHD, National Institute of Health, Bethesda, MD, USA

applications (4–14). This review focuses on the double-PFG (d-PFG) MR methodology as a probe for new and important microstructural features that may lead to new contrasts in MR imaging. First, the microstructural information available from conventional single-PFG (s-PFG) methods is briefly described, together with their limitations. d-PFG methodology is then introduced, and the various experimental aspects of the method are discussed. The potential of d-PFG to extract new microstructural information from complex specimens (arising from recent theoretical advances) is also presented. Subsequently, studies designed to validate the theoretical findings and to assess the accuracy of the microstructural information that can be extracted using d-PFG methodology are reviewed. Finally, experimental aspects and initial applications of d-PFG MRI are presented, and future prospects of the methodology are provided. It should be noted that this review focuses primarily on the experimental aspects of d-PFG; the theoretical aspects will be reviewed in due course.

s-PFG AS A PROBE FOR MICROSTRUCTURAL FEATURES

MRI provides one of the most diverse modalities for the characterization of biological tissues, and especially central nervous system (CNS) tissues (15). Distinct morphological, pathological and even functional properties can be gleaned using MRI owing to its many contrast mechanisms and high spatial and temporal resolution. Diffusion MRI (16) has become one of the most important techniques for studying neuronal tissues, as restricted diffusion can be utilized as an endogenous reporter for dimensions which are much smaller than the MRI voxel. Indeed, restricted diffusion can be used as a reporter for processes on the cellular level, an important attribute for many applications. Diffusion MRI, which can be used to report on anisotropy in the CNS (17), also reveals the pathological condition in acute cerebral ischemia where T_2 and T_1 imaging offer little information on the condition during the early stages of pathology (18); another important application of diffusion MRI in neuroscience is its ability to provide microstructural information, especially in white matter (WM), which allows tractography of the fiber bundles (8,11,16,19).

The methodology that has been most widely employed in diffusion NMR and MRI research is s-PFG (3,4,16), which uses a pair of diffusion sensitizing PFGs (or wave vectors) of magnitude and direction **G** and duration δ, which are separated by a single diffusion period Δ (note that the 'single' in s-PFG refers to a single encoding interval, comprising the two diffusion encoding PFGs). This 'diffusion block' can be inserted within a spin echo (SE) or stimulated echo (STE) sequence yielding single-pulsed gradient spin echo (s-PGSE) and single-pulsed gradient stimulated echo (s-PGSTE) experiments, respectively (Fig. 1A, B). The physical basis of the NMR signal decay in the presence of diffusion has been reviewed previously (4,20). Briefly, the first gradient pulse encodes the spins according to their positions, resulting in a spatially dependent acquired phase, whereas the second gradient pulse, applied in an opposite sense, is used to refocus the acquired phase. Stationary molecules acquire zero net phase, and the MR signal does not attenuate; on the contrary, diffusing molecules acquire some finite random net phase, which leads to phase dispersion and signal attenuation (4,20).
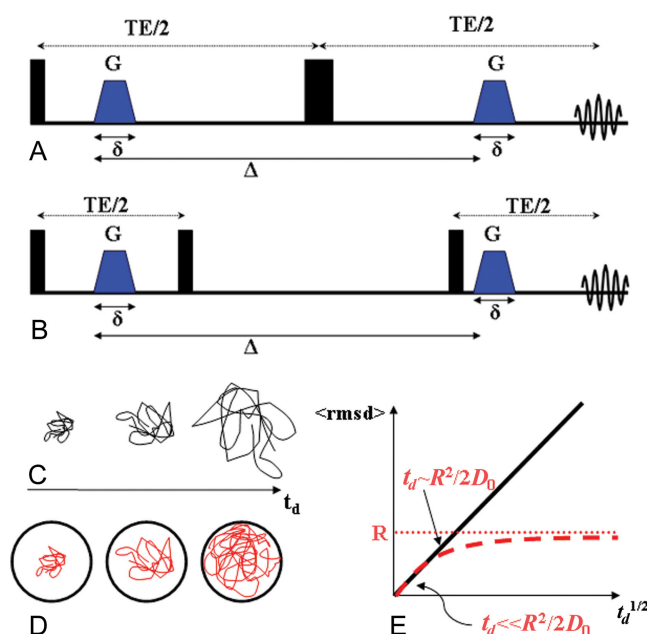

Figure 1. Single-pulsed field gradient (s-PFG) sequences and diffusion modes. (A) Single-pulsed gradient spin echo (s-PGSE) sequence. (B) Single-pulsed gradient stimulated echo (s-PGSTE) sequence. (C) Schematic representation of free diffusion for different diffusion periods. (D) Schematic representation of diffusion in a confining geometry for different diffusion periods. (E) Schematic representation of the root-mean-square displacement (rmsd) for varying diffusion periods for free (black line) and restricted (red broken line) diffusion. The red dotted line represents a quantity related to the compartment size R, and D_0 is the diffusion coefficient.

For freely diffusing spins in isotropic systems (i.e. no confinement or barriers to motion; Fig. 1C), diffusion is Gaussian and the normalized signal attenuation $E(\mathbf{q})$ obeys the expression:

$$E(\mathbf{q}) = \frac{S(\mathbf{q})}{S(\mathbf{q}=0)} = e^{-4\pi^2 |\mathbf{q}|^2 t_d D} = e^{-bD}$$

where $\mathbf{q}$ is defined as the wave vector $\mathbf{q} = (2\pi)^{-1} \gamma \delta \, \mathbf{G}$, γ is the gyromagnetic ratio and the b value is defined as $b = 4\pi^2 |\mathbf{q}|^2 t_d$, where t_d is the effective diffusion time; in the case of rectangular gradients, $t_d = \Delta - \delta/3$ (3). In such free diffusion systems, the displacement distribution is Gaussian. A logarithmic plot of $E(b)$ against the b values yields a linear dependence from which the diffusion coefficient D can be extracted. In free diffusion, 'D' is time independent; for example, for different diffusion periods, the same value of D will be extracted. The root-mean-square displacement (rmsd) of the diffusing moiety can be obtained by Einstein's relation: $(\text{rmsd})^2 = 2nDt_d$ (where $n = 1, 2$ and 3 for one-, two- and three-dimensional diffusion processes, respectively). For free diffusion, the plot of rmsd *versus* $t_d^{1/2}$ yields a linear correlation (Fig. 1E, black line). Moreover, as there are no boundaries to obstruct the diffusion process, a measurement along any direction will yield the same rmsd. This can be regarded as a free isotropic diffusion profile.

A completely different profile is obtained when impermeable barriers are introduced to the sample, forming a compartment in which restricted diffusion can take place (Fig. 1D). In this case, when the diffusion periods are sufficiently long, diffusion is no longer Gaussian as the boundaries are obstructing the diffusion process and only an apparent diffusion coefficient (ADC) can be obtained at low b values. In such a scenario, the signal decay may

lose its linearity with respect to the b value when heavier diffusion weighting is applied, and a completely different treatment of the signal decay is necessary (see 'The high q-regime: diffusion–diffraction minima and q-space approach' section). In contrast to free diffusion, the signal attenuation arising from restricted diffusion depends on both the diffusion period and, in cases of anisotropic compartments, on the direction in which the measurement is performed (21). The time dependence of the ADC arises from the fraction of molecules that sample the boundaries of the compartment at a given diffusion time and, for short diffusion periods ($t_d << R^2/2D_0$, where D_0 is the diffusion coefficient of the species and R is the radius of the compartment), the rmsd increases linearly when plotted against $t_d^{1/2}$, as a result of the very small fraction of molecules that experience the confining boundaries (Fig. 1E, red broken line). However, as Δ is prolonged, the boundaries of the compartments are gradually sampled by more and more molecules, and, when $t_d \sim R^2/2D_0$, the rmsd levels off asymptotically towards the size of the compartment (Fig. 1E, red broken line; the horizontal dotted line represents the compartment size). It should be noted that, in the case of nonspherical compartments, the direction of measurement is also important: for open cylinders, for instance, diffusion along the main axis of the cylinder will exhibit a free diffusion profile, whereas diffusion along the direction perpendicular to the main axis will exhibit a restricted diffusion profile (Fig. 1E).

This sensitivity of the signal decay towards environmental effects, coupled with the ability to probe diffusion on many length scales by prolongation of the diffusion period, is what makes diffusion MR such a remarkable probe for microstructural features. Although biological tissues and, especially, neuronal tissues are highly complex, in certain cases they adhere to the principles outlined above; therefore, diffusion measurements can be used as a source of contrast in MRI (16).

In the following sections, we focus on low- and high-q regimes, and on the different microstructural features that can be extracted in the two regimes.

The low-q regime and diffusion tensor imaging (DTI)

Let us consider an array of cylindrical compartments coherently packed with their principal axes along the z direction. The anisotropy of the cylinders can be inferred from inspecting the ADCs in the x and z directions, obtained from s-PFG measurements at low q values, where the signal can still be approximated to represent Gaussian diffusion. In this case, $ADC_x < ADC_z(= D_0)$ will be obtained, as diffusion is restricted in the x direction and free in the z direction. It should be noted that such a result will be obtained only for Δ sufficiently long to probe the boundaries; we therefore purposefully make the distinction between low q values and low b values for restricted diffusion [a low b value may comprise a combination of extremely short Δ and strong gradients, where the molecules will hardly probe the boundaries of the restricting compartments; therefore, a misleading isotropic profile ($ADC_x = ADC_z(= D_0)$) might be observed for a cylindrical compartment].

Although the idea that ADC should actually be treated as a tensor quantity was understood by many, Basser *et al.* (19) proposed the mathematical framework and experimental design to measure this quantity, which led to DTI. In DTI, the diffusion tensor components can be extracted from diffusion measurements in (at least) six spatial directions using low q values and with Δ sufficiently long to probe the boundaries of the compartment. As the principal diffusivities of the tensor are invariant to rotation, they represent intrinsic quantifiable parameters. They can be used to derive yet other parameters that quantify the anisotropy of the compartments, such as fractional anisotropy (FA) or relative anisotropy (RA). Utilizing the principal directions, the orientation of the compartments in space can also be inferred from DTI. DTI has been highly exploited in biomedicine, enabling, *inter alia*, a remarkable new contrast between WM and other CNS components, such as gray matter (GM) and cerebrospinal fluid (CSF), and offering the possibility of fiber tracking [for comprehensive reviews on DTI, see refs (7,8,11,16,22)]. It should be noted that other schemes of treating the diffusion tensor, such as quadratic form analysis, exist (23). Through its treatment of diffusion at low q values, DTI offers a remarkable tool for studying and quantifying *directional* information of microstructures, albeit not offering measures of compartment size.

The high-q regime: diffusion–diffraction minima and the q-space approach

Diffusion tensor analysis requires that DTI use only the low-q part of the signal decay as it assumes Gaussian diffusion and a single diffusing component. However, it is a well-established fact that the signal decay arising from restricted diffusion in confined compartments is non-monoexponential at higher q values (10,12,24–26) and that, in the case of biological tissues, more than a single diffusing component exists. Importantly, this non-monotonicity of the signal decay offers the possibility of extracting different microstructural parameters from those offered by DTI, and especially pore size.

Diffusion–diffraction minima

When the specimen contains compartments of the same size and a diffusion measurement is conducted such that high q values are reached in the restricted direction and Δ is sufficiently long to probe the restricting boundaries, diffusion–diffraction troughs may be observed in the E(q) plots (27). Importantly, the size of the compartment can be derived from the diffusion–diffraction troughs (28) when the pore geometry is known and, for nonspherical (i.e. anisotropic) infinite cylindrical compartments, the diffraction-like patterns show a strong dependence on the rotational angle between the principal axis of the compartment and the orientation of the gradients, affording microstructural information about compartment directionality (29,30). In recent years, the theoretical background for such phenomena has been advanced for various geometries (28,30–33), and these NMR diffusion–diffraction troughs have been observed experimentally in systems which are characterized by compartments with relatively monodisperse sizes, such as narrowly distributed emulsions (34), solvent diffusing in polymer cavities (35), water-filled microcapillaries (29,30,36,37) and even red blood cells (RBCs) (38–46). The ability to observe diffusion–diffraction minima in RBCs, for example, provides an extraordinary noninvasive method of exploring these cells, including size and shape, permeability and even dynamic processes (45). To account for the effect of numerous experimental parameters on the shape and location of the diffusion–diffraction troughs, well-controlled systems in which the 'ground-truth' is known *a priori* were studied and the findings could be realized theoretically (29,30,36). In cases in which the diffusion–diffraction troughs disappear as a result of susceptibility effects induced by

inhomogeneities of the sample, it has been shown that, using radiofrequency (RF) gradients (35) or bipolar gradients (37), one can recover the diffraction-like features, and therefore extract the relevant microstructural information from the sample.

It is important to note that the observation of diffusion–diffraction troughs is critical in the sense that it bears a signature for restricted diffusion, a property which is not always easily inferred in s-PFG experiments.

q-space approach

Compared with DTI, diffusion–diffraction troughs can offer new microstructural information about the compartments, namely the compartmental dimensions. However, diffusion–diffraction minima are generally not observed in most diffusion measurements in biological systems (see 'Limitations of s-PFG methodology' section) and, in such cases, the signal decays smoothly (but non-monoexponentially) with increasing q values (10,24,25). In such cases, the q-space approach offers yet another possibility of inferring compartmental dimensions. In the q-space approach, one makes use of the Fourier relationship between smooth $E(q)$ data (measured up to high q values) and the diffusion propagator $\tilde{P}$ (47) [see ref. (48) for a treatment of the propagator for nonsmooth $E(q)$ data such as those that arise in RBCs]. When smooth $E(q)$ data are Fourier transformed, the displacement probabilities can be obtained and the averaged rmsd of the diffusing moiety can be extracted. In completely free and unconfined systems, the displacement probability is characterized by a mono-Gaussian function (as the propagator is in fact Gaussian). In complex specimens, such as neuronal tissue, the smooth $E(q)$ signal decay is often approximated by a decay of two components (fast and slow), which are manifested as a superposition of two probability distribution functions (PDFs) in the Fourier transform of $E(q)$. In some cases, these two PDFs have been approximated by a bi-Gaussian function (10,24,25,49). The rmsd of the fast and slow components extracted from the bi-Gaussian function can then be used to characterize different microstructural features of the sample, such as different length scales in the tissue, although it remains extremely difficult to assign these components to specific cellular compartments, and such a model assumes Gaussian diffusion even for the restricted component. Another useful property of the q-space approach in these cases is that the fast diffusing components of the signal decay can be suppressed by using very long Δ, and slowly diffusing components can be accentuated. For example, the slow component extracted from excised optic nerve has been shown to provide a good estimate of the mean axon sizes, as well as an accurate means of extracting the directionality of the fiber (50,51). The q-space approach, reviewed in this issue (52), has been shown to provide complementary microstructural information to DTI, and has been used in a variety of applications, such as studies of myelin-deficient rats (53,54), the detection of multiple sclerosis (25,55) and even differentiation between vascular dementia and Alzheimer's disease (56). A recent study by Ong *et al.* (57), employing extremely strong gradients in excised spinal cord, provided a striking example of the potential usefulness of the size characterization: in this study, excellent contrast between distinct morphological regions, corresponding to regions of varying average diameters in histology, was achieved, and the microstructural information obtained by the q-space approach far exceeded in its breadth that available from DTI (57). Other studies measuring compartment sizes offered

improved sensitivity to morphological features in normal tissue (58,59), and to neuropathological conditions, such as spinal cords of pigs with experimental allergic encephalomyelitis (60), as well as in myelin-deficient rats (53). Such studies provide a 'virtual histology' of a specimen under investigation. Therefore, the q-space approach offers different microstructural information from DTI, namely the relative compartment sizes in which restricted diffusion takes place.

Figure 2 illustrates schematically the different microstructural information that can be retrieved from the different q regimes from a neuronal-like structure. Figure 2A shows an illustration of two adjacent MR voxels, each containing a pack of perfect parallel impermeable cylinders which have similar inner diameters, namely 5 and 6 µm, representing two different adjacent WM bundles. Figure 2B shows simulations for $E(q)$ data in both z and x directions from the low-q regime, assuming that Δ is sufficiently long to probe the boundaries and δ is negligible, i.e. the short gradient pulse (SGP) approximation is fulfilled. The broken line points to the q value in which a typical DTI experiment is carried out (corresponding to $b = 1000 \text{s/mm}^2$ with $\Delta = 40$ ms). As shown in Fig. 2B, at low q values, the signal decay in the x direction is almost identical for the two cylinders, while, in the z direction, spins are unhindered, enabling larger phase accumulation and consequently stronger attenuation of the signal (Fig. 2B). The reason that the signal decay in the x direction is so similar between the two different packs at the low q-regime is a result of the long length scale which is probed at low q values. However, when higher q values are reached, the diffusion–diffraction troughs can be observed at $q = 2037 \text{ cm}^{-1}$ and $q = 2437 \text{ cm}^{-1}$ for cylinders with inner diameters of 6 and 5 µm, respectively (Fig. 2C), affording a way to easily resolve the size of each cylinder.

The microstructural information available from the DTI measurement reveals the orientation of the cylinders for both voxels (as diffusion in the x and z directions is different), truthfully depicting the ensemble anisotropy (EA) present in both voxels, as could be, for example, manifested in FA maps (Fig. 2D); however, two such voxels would be almost indistinguishable from one another as the information about the size of the compartment is unavailable at low q values. In contrast, the microstructural information from q-space analysis of the data will indeed reveal the distinct sizes of the compartments; therefore, contrast can be achieved between the two voxels (Fig. 2E). Thus, different and complementary microstructural information is gathered from the two methodologies.

Limitations of s-PFG methodology

Although s-PFG methodology can be exploited in a variety of applications, it has its limitations, some of which are inherent to the methodology and some of which are technological in nature, precluding important microstructural information from being obtained. The inherent limitations of s-PFG arise from the introduction of distributions (either orientation or size) in the specimen.

1. In the high-q regime, the diffusion–diffraction troughs, together with the vast microstructural information that they can convey, are easily lost as a result of size polydispersity (see section on the 'Robustness of zero-crossings in size distribution phantoms'). Most realistic diffusion systems, such as axons in WM, but also emulsions and rocks, are indeed almost always characterized by size distributions. Therefore, in almost every 'real' application of q-space spectroscopy or imaging,
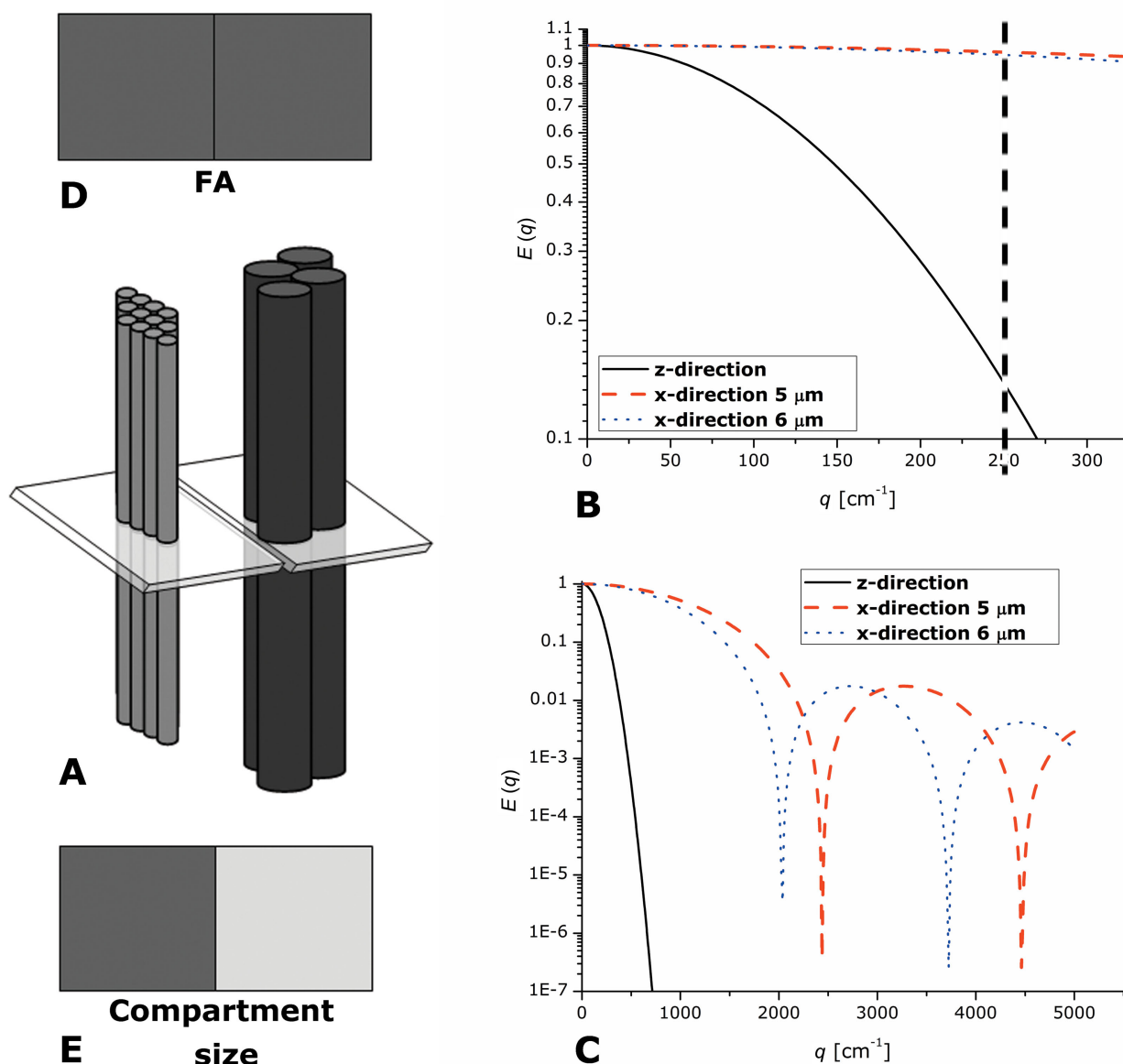
Figure 2. Complementary microstructural information available from diffusion tensor imaging (DTI) and q-space methodologies in the different q regimes. (A) Schematic representation of two MRI voxels passing through two ensembles of cylinders with inner diameter (ID) = 5 and 6 μm (light gray and dark gray, respectively). (B) Simulated $E(q)$ plots for low q values for diffusion in the z direction (free) and for each ensemble of cylinders in the x direction (restricted). The simulations assume the short gradient pulse approximation with $\Delta = 40$ ms, sufficiently long to probe the boundaries in the restricted direction. At low q values, the two ensembles produce almost identical signal decay and are almost indistinguishable from one another. (C) Simulated $E(q)$ plots for high q values for diffusion in the z direction (free) and for each ensemble of cylinders in the x direction (restricted). Note the diffusion–diffraction minima for each ensemble. The diffusion–diffraction minima occur at $q = 2437$ and $q = 2037$ cm^{-1} for ID = 5 and 6 μm, respectively. (D) Schematic representation of microstructural information as depicted by DTI – for the two MRI voxels, anisotropy is observed at low q values as depicted by the fractional anisotropy (FA) values; however, the voxels convey identical information because of the inability of DTI to resolve sizes at low q values. (E) Schematic representation of microstructural information as depicted by the q-space approach– each MRI voxel will have a different intensity as the q-space approach can resolve the sizes from the diffusion–diffraction minima.

the diffusion–diffraction minima are lost, and one must resort to the q-space approach, which may yield an averaged and somewhat relative compartment size, especially when one is forced to use finite and long δ.

2. Specimens which are characterized by locally anisotropic compartments that are randomly oriented will exhibit overall isotropy when measured in s-PFG methods (i.e. diffusion measured in any orientation will generate an identical signal decay, which will yield equivalent eigenvalues in DTI). Impor-

tantly, such structures may be present in GM, where neurons and dendrites are randomly aligned in space. In such cases, DTI measurements will yield zero anisotropy (as a result of the averaging of diffusion directors in all directions), thereby losing important microstructural information. Interestingly, in such cases, it can be difficult to even infer on the presence of restricted diffusion, as diffusion–diffraction minima are lost, together with the microstructural information obtained there-from.

Figure 3 presents different scenarios for restricted diffusion, together with the microstructural information that can be obtained in each case using s-PFG methodologies. An illustration of an ensemble of monodisperse spherical pores is shown in Fig. 3A. At low q values, DTI will produce equal eigenvalues, and an isotropic profile will be obtained. The ADC that can be extracted may be lower than that of free water, but that, in itself, does not necessarily imply on restricted diffusion. However, at high q values, the diffusion–diffraction troughs are observed in all directions, which means that the presence of restricted diffusion can be ascertained, and both the size of the compartment and the fact that it is spherical can be inferred. Figure 3B shows an ensemble of coherently placed cylinders. Here, the anisotropy of the compartment can be extracted by both DTI and q-space analysis, with the latter also offering the compartment size.

When size distributions are introduced to the compartments (Fig. 3C), DTI will still be able to convey the anisotropy of the cylinders; however, at the high-q regime, the diffusion–diffraction minima will be lost as a result of the size distribution, and the size

of the compartment will no longer be available from the diffusion–diffraction troughs. When a size distribution is introduced to spherical compartments (Fig. 3D), an isotropic profile will be obtained from DTI, from which it may be difficult to infer restricted diffusion in the spherical compartment; however, one may infer the presence of restricted diffusion from non-monoexponential signal decay at the high-q regime. Figures 3E and 3F show randomly oriented cylindrical and ellipsoidal compartments, respectively. Such compartments are locally anisotropic but macroscopically isotropic. For both cases, neither DTI nor high-q experiments will convey useful microstructural information; DTI will extract an isotropic profile, and the diffusion–diffraction minima will be lost; neither method is able to distinguish between randomly oriented ellipsoids and randomly oriented cylinders, or to provide microstructural information characterizing the compartments, such as eccentricity in ellipsoids or length/diameter ratios in cylinders.

Three distinct mechanisms of anisotropy have been introduced recently by Özarslan (61) to describe the scenarios presented
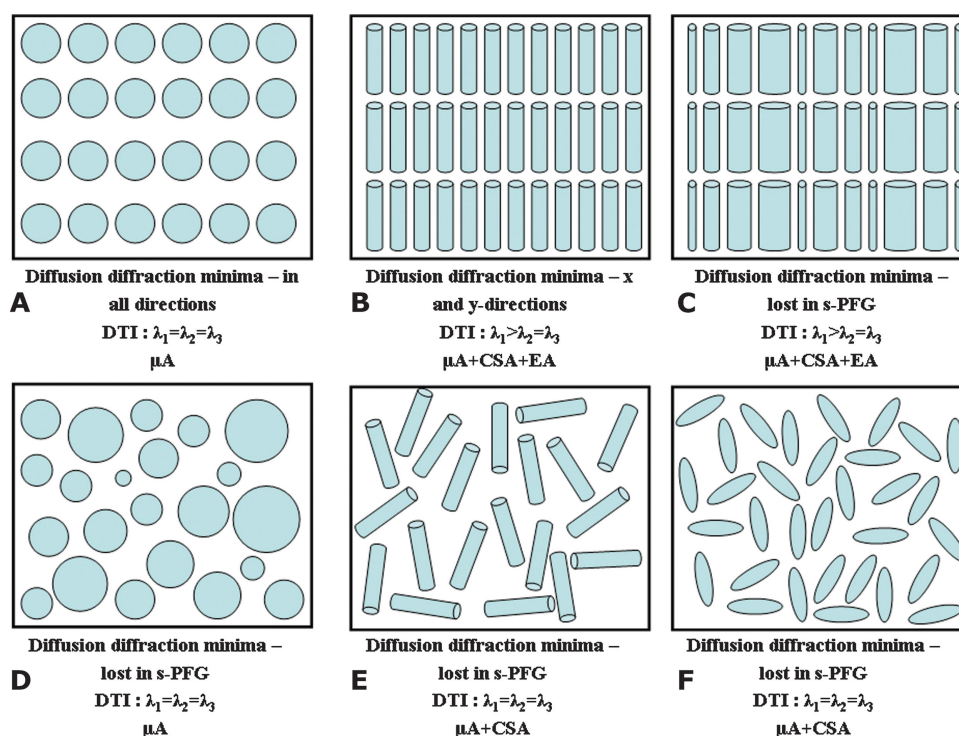

Figure 3. Restricted diffusion in various compartmental scenarios, the microstructural parameters that are available from single-pulsed field gradient (s-PFG) experiments and the types of anisotropies present. (A) A schematic representation of an ensemble of monodisperse spherical compartments. Generally, it may be very difficult to infer on restricted diffusion in such cases using diffusion tensor imaging (DTI). At higher q values, the diffusion–diffraction minima will appear in all directions, conveying that this system is indeed characterized by restricted diffusion. The diffusion–diffraction minima also enable inference on the spherical nature of the compartments. In this case, microscopic anisotropy exists, arising from the boundaries of the compartments. (B) A schematic representation of monodisperse cylindrical compartments coherently aligned in a certain direction. Note that, as the compartments are cylindrical and nonpermeable, compartment shape anisotropy (CSA) also exists, as does microscopic anisotropy; as the cylinders are coherently packed, ensemble anisotropy (EA) also exists in this scenario. DTI parameters will be able to convey the EA of the sample. The diffusion–diffraction minima will appear in the restricted direction, from which the size of the monodisperse microcapillaries will be extractable. (C) A schematic representation of coherently packed cylindrical compartments characterized by a size distribution. The same types of anisotropy are present as in (B); DTI parameters will be able to extract the EA of the sample. The diffusion–diffraction minima, however, are lost, together with the important microstructural information they convey. (D) A schematic representation of spherical compartments characterized by a size distribution. In this case, the diffusion–diffraction minima are lost, and the presence of restricted diffusion will be hard to infer. As in (A), only microscopic anisotropy exists for this sample, as it is spherical. (E) A schematic representation of randomly oriented compartments of cylindrical shape. (F) A schematic representation of randomly oriented ellipsoids. In both (E) and (F), the s-PFG methodologies will not be able to extract meaningful microstructural information. In both (E) and (F), both microscopic anisotropy and CSA exist, but s-PFG methods cannot distinguish between the two. The CSA in (E) is different from that in (F) as the compartments are cylindrical and ellipsoid, respectively.

Copyright © 2010 John Wiley & Sons, Ltd.   *NMR Biomed.* 2010; **23**: 757–780

above: (i) microscopic anisotropy that arises from the boundaries of restricted compartments, even when they are spherical; (ii) compartment shape anisotropy (CSA) that arises from the shape of the compartments; and (iii) EA, which arises from the coherence of packing of locally anisotropic pores. It should be noted that s-PFG methods are most useful to measure anisotropy when EA is present in the specimen.

Other s-PFG limitations are mostly technological and indicate the need for strong gradient systems.

1. The first diffusion–diffraction trough of monodisperse compartments occurs at the q value that corresponds to the reciprocal of the size of the compartment [corrected to a geometrical factor (28,38)]. Therefore, the smaller the compartmental size, the higher the q value of the diffusion–diffraction trough. As the SGP condition must be met for the diffusion–diffractions to have sharp minima at the accurate q value, s-PFG methodology suffers from a need for extremely strong gradient amplitudes that require adequate hardware. Even when diffusion–diffractions are not observed, such as in most biological tissues, rocks, emulsions and other porous media (typically characterized by sizes smaller than 5 μm), very high q values must be reached to accurately carry out the q-space approach, and very strong gradients are needed, as it is favorable to remain in the SGP regime (57). This need for very strong gradients therefore limits the applicability of s-PFG methodology despite the important microstructural information that can be obtained.

2. In the high-q regime, the signal-to-noise ratio (SNR) is low because of strong diffusion weighting. Coupled with the need to measure several q values, and possibly even in several spatial directions, q-space methodology is relatively time-consuming, although fast diffusion measurements (45,62) or measurements that can be conducted at lower q values to estimate compartment size (63) are emerging. Moreover, where diffusion–diffraction patterns are not observed, extraction of sizes from the q-space approach is amenable to averaging of the sizes sampled by the diffusing species, and does not convey information that would yield properties of the size distribution itself.

In the following sections, we review d-PFG methodologies and the possibilities that they offer to overcome some of the inherent limitations of s-PFG.

d-PFG METHODOLOGY AS A PROBE FOR MICROSTRUCTURES

Methodology

d-PFG methodology employs two diffusion sensitizing gradient pairs, $\mathbf{G_1}$ and $\mathbf{G_2}$, with durations δ_1 and δ_2, respectively, that are separated by a mixing time t_m. Two diffusion periods, namely Δ_1 and Δ_2, exist in the interval between each gradient pair. The corresponding $\mathbf{q}$ vectors for the two encoding blocks can be considered as $|q| = |\mathbf{q_1}| = |\mathbf{q_2}|$, where $\mathbf{q}_i = (2\pi)^{-1}\gamma\delta \mathbf{G}_i$. The d-PGSE sequence is shown in Fig. 4A, specifying all of the experimental parameters. A variant of d-PGSE is shown in Fig. 4B, in which the two inner gradients (the second $\mathbf{G_1}$ and the first $\mathbf{G_2}$) are superposed, so that t_m is effectively zero – a desirable

condition for several applications (see below). It should be noted that, in these sequences, the diffusion periods occur when magnetization is in the X–Y plane, rendering the sequence vulnerable to T_2 relaxation. To avoid signal loss owing to T_2 relaxation, the 180° RF pulses can be decomposed into pairs of 90° pulses, which then allow z storage of the magnetization during different intervals, yielding d-PGSTE sequences. Two such variants of d-PGSTE, one in which a finite t_m exists and one in which t_m is zero, are shown in Fig. 4C and 4D, respectively. Other variants of d-PFG methodology exist, such as the seven 90° pulse sequence which allows for prolongation of the mixing time when the magnetization is in the z direction, as well as other variants (64). It should also be noted that, as a natural extension to s-PFG and d-PFG methodologies, multiple-PFG experiments can be devised, in which further diffusion blocks are added (65).

d-PFG methodology offers many degrees of freedom, namely the orientations and strengths of each of the individual gradients, as well as the diffusion periods that can be separately varied, and the mixing time. An important and unique feature of d-PFG is the variable angle between the gradient pairs, $\mathbf{G_1}$ and $\mathbf{G_2}$, denoted ψ (Fig. 4E). Figure 4E also defines the polar and azimuthal angles θ and φ, respectively. These many degrees of freedom offered by d-PFG enable many different acquisition schemes. First, one can fix the diffusion periods as equal ($\Delta_1 = \Delta_2$) and gather $E(q)$ data by increasing both of the q values (usually concomitantly) with a fixed angle ψ between the gradients. When anisotropic compartments are probed, it is convenient to denote special cases of angle pairs: for example, an experiment conducted with $\mathbf{G_1}$ in the x direction and with the angles $\theta = 90°$ and $\varphi = 0°$ between the gradient pairs can be denoted d-PFG$_{xx}$; the indices indicate that $\mathbf{G_1}$ and $\mathbf{G_2}$ are collinear and both in the x direction. Similarly, the special cases with $\mathbf{G_1}$ in the x direction and $\theta = 90°$ and $\varphi = 90°$ or with $\mathbf{G_1}$ in the z direction and $\theta = 90°$ and $\varphi = 0°$ can be denoted d-PFG$_{xy}$ and d-PFG$_{zx}$, respectively; such experiments can be referred to as orthogonal experiments. Many combinations of such experiments can be carried out by varying the diffusion periods (concomitantly or independently) or the mixing time for each pair of directions.

A second and very different type of acquisition scheme involves the d-PFG angular experiment. In such experiments, the diffusion periods and t_m are fixed, and the angle ψ between the gradients is varied for a certain q value. For anisotropic, cylindrical compartments with their principal axes aligned in the z direction, it is instructive to consider a measurement in the X–Y plane, i.e. $\mathbf{G_1}$ is set in the x direction with $\theta = 90°$ and $\varphi = 0°$ and the orientation of $\mathbf{G_2}$ is varied between $\varphi = 0°$ and 360° in the X–Y plane (Fig. 4F). Such angular dependences can also be repeated with varying diffusion periods or mixing times, and for multiple q values.

Other acquisition schemes exist, such as two-dimensional d-PFG, where the diffusion periods are fixed and, for each value of $\mathbf{q_1}$, the whole spectrum of $\mathbf{q_2}$ is acquired; in such cases, a two-dimensional diffusion–diffusion correlation map can be obtained for different values of diffusion periods and/or mixing times (66).

Early d-PFG experiments and theory

As mentioned earlier, one of the limitations of s-PFG occurs when anisotropic compartments are randomly distributed such that, macroscopically, they appear isotropic in s-PFG measurements because of the averaging of directors within the MR voxel (as depicted in Fig. 3E, F). Indeed, in such cases, it may be extremely
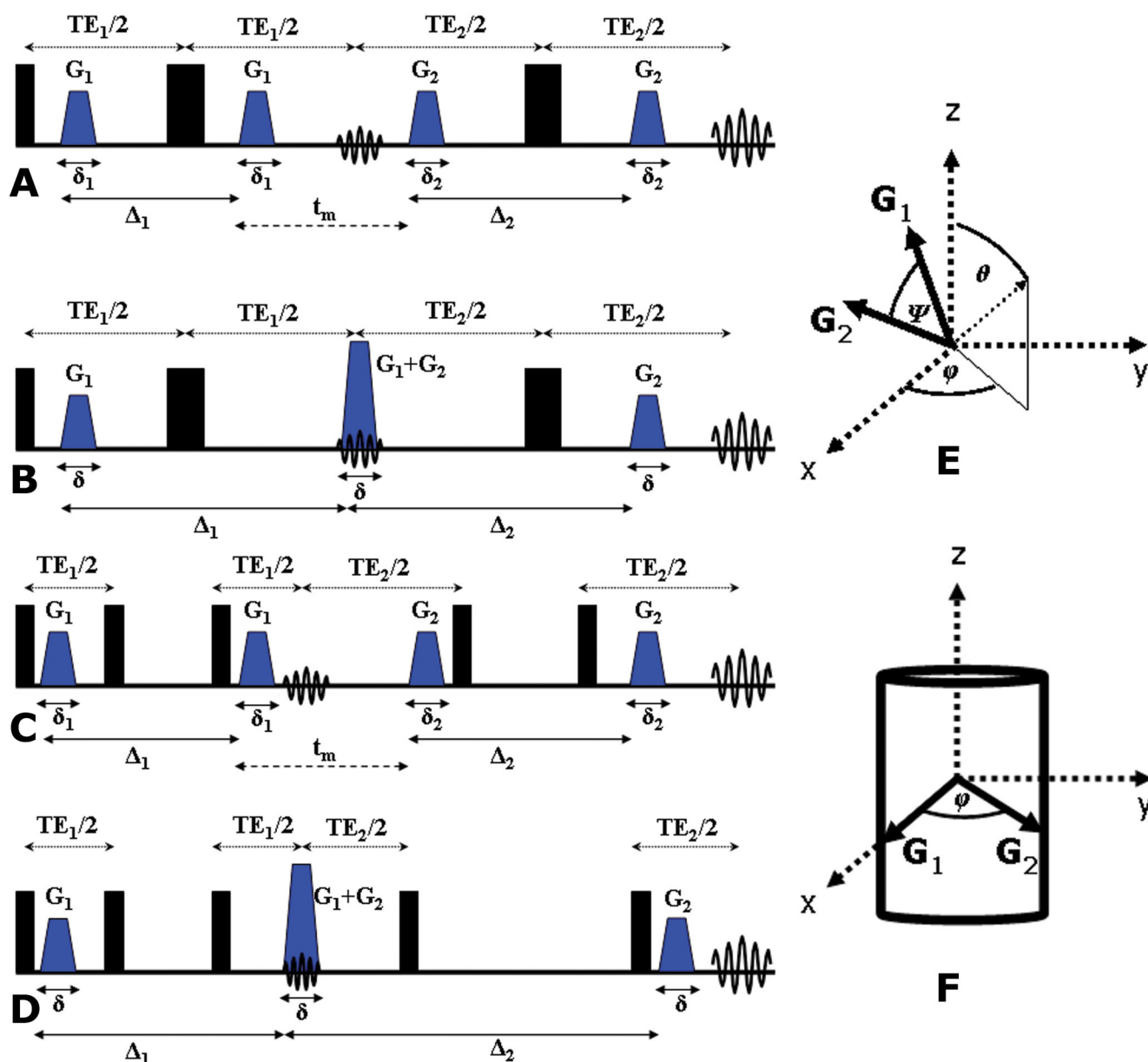
Figure 4. Double-pulsed field gradient (d-PFG) sequences and orientation schemes. (A) Double-pulsed gradient spin echo (d-PGSE) with finite mixing time. (B) d-PGSE with $t_m = 0$ ms, where the middle gradients are superimposed. (C) Double-pulsed gradient stimulated echo (d-PGSTE) with finite mixing time. (D) d-PGSTE with $t_m = 0$ ms, where the middle gradients are superimposed. (E) Definition of the angle ψ between the two gradient pairs. The angles θ and φ are also defined. (F) The d-PFG angular experiment. Generally, G_1 can be set in any direction and the angle ψ is varied between the gradient pairs. In the variant shown in (F), G_1 is set in the x direction, with $\theta = 90°$, and the orientation of G_2 is varied along the angle φ (i.e. in the $X-Y$ plane). Narrow and white black boxes represent $\pi/2$ and π pulses, respectively.

difficult to even infer the presence of restricted diffusion, and s-PFG methodologies can extract microstructural information only in coherently placed compartments (Fig. 3A, B). In 1990, Cory et al. (67) used the seven 90° pulse d-PGSTE variant to probe diffusion and spin transport in randomly oriented eccentric yeast cells. In this study, Cory et al. compared displacement profiles [obtained from Fourier transform of $E(q)$ data] from two different d-PFG experiments, one in which G_1 and G_2 were collinear, and one in which G_1 was orthogonal to G_2 (d-PGSTE$_{xx}$ and d-PGSTE$_{xy}$, respectively). It was demonstrated that the displacement profile in a d-PGSTE$_{xx}$ experiment was different from that in a d-PGSTE$_{xy}$ experiment (67). Thus, Cory et al. were

able to infer from d-PFG experiments that the yeast cells were microscopically anisotropic. On the contrary, s-PFG acquisitions along any direction yielded isotropic displacement profiles, which could lead one to the erroneous inference that the cells are spherical. The novelty of the methodology introduced by Cory et al. was the use of d-PFG collinear and orthogonal measurements to infer the eccentricity of randomly oriented yeast cells, a microstructural property that was completely lost in s-PFG.

The reasons for the different signal decays in collinear and orthogonal d-PFG experiments were later elucidated in a theoretical study of the signal decay in d-PFG conducted in

1995 by Mitra (68). Mitra studied theoretically the signal decay arising from restricted diffusion in an ensemble of pores using the d-PGSE sequence in the low-q regime and under idealized conditions of $\delta \to 0$, $\Delta \to \infty$ and $t_m \to 0$ or $t_m \to \infty$. Mitra found that, when the angle ψ between $\mathbf{G_1}$ and $\mathbf{G_2}$ is varied (as in the experiment depicted in Fig. 4F), the signal decay follows a bell-shaped function, even when the pores are spherical. This observed anisotropy in the spherical pores implied a new mechanism for anisotropy, namely microscopic anisotropy, which is induced by the boundaries of the confining geometry. In an outstanding theoretical insight, Mitra predicted that this $E(\psi)$ angular dependence could be used to detect anisotropy that arises from the boundaries of the restricting geometry, even in randomly oriented anisotropic compartments (Fig. 3E, F) (68). Mitra's study predicted that, for $t_m \to 0$, the angular dependence of the signal decay would hold for any compartment shape, including spherical compartments. In this study, Mitra presented a way to differentiate between the situation shown in Fig. 3A (spherical pores) and Fig. 3E, F (randomly oriented nonspherical compartments). At $t_m \to \infty$, the angular dependence was predicted to be preserved only for randomly oriented compartments that were nonspherical, i.e. the signal decay exhibits anisotropy as a result of compartment shape [later coined 'compartment shape anisotropy' (CSA)]. Indeed, Mitra's theory (68) suggested a new tool for obtaining a signature for restricted diffusion even in randomly oriented compartments at the low-q regime, an extremely desirable property for many applications, especially of clinical relevance.

Cheng and Cory (69) were able to delineate eccentricities in different types of yeast cell at long mixing times by again comparing the displacement profiles from collinear and orthogonal high-q-value d-PFG experiments (which correspond to only two values of ψ in the angular dependence of the signal decay). In another study, Callaghan and Komlosh (70) used the same approach to study the signal decay in lyotropic liquid crystals, which can be approximated by microscopic cylindrical compartment domains randomly distributed within the crystals; later, Komlosh et al. (71) extended this approach to a GM phantom and then to monkey GM, and to spinal cord d-PFG-weighted imaging (72). It should be noted that, in all of the above studies, s-PFG measurements yielded an isotropic signal decay because of the macroscopic isotropy of the specimens (see the 'Theory' section). d-PFG, therefore, offered microstructural information that could not be accessed by s-PFG measurements. In all of the above studies, the full angular dependence was not studied, but only collinear and orthogonal d-PFG measurements were compared as a means to infer the local properties of the randomly oriented compartments.

Other d-PFG methodologies, in which different experimental and analytical schemes were employed, have been used in a range of different applications which are beyond the scope of this review: d-PFG variants were shown to be able to suppress the solvent signal (73) and convection artifacts (74,75) in diffusion measurements. Different variants of d-PFG can be used in two-dimensional acquisition schemes to infer correlation of flow and dispersion phenomena (76,77), and molecular migration and exchange in porous media (66,78–81).

Several recent studies have used Mitra's theory to analyze the angular dependence in d-PFG imaging experiments conducted on several specimens (82–84) (see the 'd-PFG MRI' section) and in Monte Carlo simulations of d-PFG in restricted pores (85–88). In the following section, a brief theoretical description is given of the theory pertaining to d-PFG experiments, from Mitra's first study to the recent developments in the theory.

THEORY

In this section, we briefly review the theoretical developments that aim to predict the diffusion-attenuated MR signal in d-PFG experiments. As the theory developed to account for the wealth of features provided by the d-PFG acquisitions is rather elaborate, we briefly summarize the milestones pertaining to the effects of restricted diffusion in a mostly qualitative fashion. The reader is urged to refer to the cited references for a more detailed picture.

As mentioned above, d-PFG MR was introduced by Cory et al. (67) as an extension of the two-pulse Stejskal–Tanner experiment. Although the authors provided no theoretical treatment, this work yielded the essential insight that the eccentricity of anisotropic compartments could be characterized via such sequences.

The existing theoretical studies can be cast into three classes based on the experiment being performed: angular, radial and arbitrary acquisitions.

Theory of angular d-PFG

In angular d-PFG, the angle between the gradients is varied whilst keeping their magnitude fixed. The influence of restricted diffusion on angular d-PFG MR acquisitions was studied systematically for the first time by Mitra (68). The main goal of Mitra's work was to lay the foundation for the interpretation of such experiments. In this seminal work, a Taylor series expansion of the d-PFG signal was considered, and a number of simplifying assumptions were made in the timing parameters. Specifically, the duration between the gradients of each PFG block was assumed to be long, and the gradient pulses were assumed to be infinitesimally short. In addition, Mitra considered two limiting cases for the mixing time. All these assumptions can be summarized in mathematical terms as follows:

- $D\Delta >> a^2$, where 'a' is the characteristic dimension of the compartment;
- $D\delta << a^2$, or the so-called 'SGP' regime;
- $\gamma \delta G a = 2\pi q a << 1$; it should be noted that this condition is implied because the theory is based on a Taylor series representation of the MR signal;
- (i) $Dt_m >> a^2$ or (ii) $Dt_m << a^2$.

Mitra predicted that, at long mixing times [condition (i)], the signal obtained for spherical pores is not expected to have any angular dependence. However, for ellipsoidal pores, an angular dependence was predicted in the fourth-order term of the Taylor expansion. Clearly, this suggests that ellipsoidal pores can be distinguished from spherical pores, supporting the view in ref. (67). Although an angular dependence was predicted, the functional form of that dependence was not provided in ref. (68).

Subsequently, Cheng and Cory (69) tackled the same regime and showed that, for a specimen comprising a randomly oriented collection of spheroidal pores (ellipsoids of revolution), the quadratic term of the signal attenuation is indeed the same when the two gradients of the d-PFG sequence are applied along parallel or perpendicular directions. Moreover, the difference

between the signal attenuations was predicted to be:

$$\Delta E = E(\psi = 0°) - E(\psi = 90°)$$

$$= \frac{2(2\pi q)^4}{375}(b^2 - c^2) + O[(2\pi qa)^6] \qquad [1]$$

where ψ is the angle between the gradients of the two encoding blocks and the semi-major radii of the spheroid are denoted by b and c. Finally, a is the longest end-to-end distance inside the pore, which is larger than b and c for the case of spheroids.

More recently, the same long mixing time regime was considered by Özarslan (61) and, *inter alia,* the full angular form of the signal profile was derived for randomly oriented spheroids as well as capped cylinders. In both cases, the fourth-order term was shown to be characterized by a $\cos(2\psi)$ dependence. These findings are consistent with Mitra's findings, as well as those of Cheng and Cory [eqn [1]], making it possible to characterize the eccentricity (CSA) of the compartments from d-PFG MR data wherein ψ values are sampled in an arbitrary fashion. Moreover, in ref. (61), a sophisticated framework was employed (see below) through which CSA can be characterized via d-PFG acquisitions with completely arbitrary parameters, thus obviating all of the conditions listed above.

The main contribution of ref. (68) is the prediction for the opposite case of short mixing times [condition (ii)]. Mitra showed that, when the mixing time vanishes, even the second-order term of the signal decay will have an angular dependence, as can be seen in the relationship:

$$E = 1 - \frac{(2\pi q)^2}{3} < r^2 > (2 + \cos\psi) + O[(2\pi qa)^4] \qquad [2]$$

where $<r^2>$ is a quantity related to the mean-square radius of gyration of the pores.

As recognized by Mitra, this is a remarkable finding that provides a signature for restricted diffusion at very low gradient strengths – a requirement critical for most clinical applications. Moreover, as such an angular dependence is not expected for multi-Gaussian diffusion processes, the observation of the angular dependence of the MR signal enables one to distinguish such processes from restricted diffusion. The subsequent development by Özarslan and Basser (89) provided a number of crucial results related to such experiments. First, the signal attenuation for free diffusion in d-PFG acquisitions with completely arbitrary experimental parameters was derived. It was shown that, for the experiment illustrated in Fig. 4A or 4C, in which a finite mixing time exists, no angular dependence is expected. On the other hand, when the two gradients at the center are superposed (as in Fig. 4B or 4D), there is some angular dependence of the signal. However, this angular dependence appears in the opposite sense to that for restricted diffusion, and hence it does not compromise the specificity of the angular patterns. Moreover, such an inverted angular dependence for free diffusion is predicted only when the pulse durations are comparable with pulse separations, i.e. $\delta \sim \Delta$.

Before discussing the treatment of restricted diffusion in ref. (89), it is worthwhile pointing out that restriction induces diffusion anisotropy even when the shape of the compartment is isotropic. This is clearly demonstrated in ref. (90), wherein it was shown how the anisotropy induced by macroscopic boundaries can be captured by s-PFG acquisitions, which is possible only when the image voxel is larger than the pore size. This is the type of anisotropy prevalent in the magnetization density profile within the pore space. When the pore size is smaller than the

voxel size, the s-PFG acquisitions lose their sensitivity to such anisotropy. The angular dependence in d-PFG acquisitions with short mixing times, as demonstrated in eqn [2], is a consequence of the anisotropy within the pore space as well. Therefore, Özarslan and Basser referred to such anisotropy as 'microscopic anisotropy' (61) to make the distinction from the anisotropy caused by the shape of the compartments clear.

To solve the problem for restricted diffusion, Özarslan and Basser employed a novel idea. In this approach, a completely general MR gradient waveform was envisioned to be composed of a train of impulses, as proposed previously in ref. (91). Unlike this work, however, in ref. (89), the authors considered the limit as the intervals between the consecutive impulses shrank, and the number of impulses approached infinity. This scheme, akin to the path integral methods in different areas of physics, enabled the analytical evaluation of the second-order term in the MR signal intensity for diffusion taking place between parallel plates, and within infinite cylinders and spheres.

Although the results are valid for any pulse sequence, Özarslan and Basser applied the formalism to d-PFG acquisitions, which led to a series of important results. First, eqn [2] was generalized to arbitrary timing parameters of the sequence. Second, it was shown how the orientation of the cylindrical fibers (when EA is present) can be estimated, together with the fiber diameter – a potentially important result for the characterization of WM when the fiber direction is unknown *a priori*. In this work, a general treatment of EA was also presented, and explicit results for randomly distributed pores were derived. It was shown how these results for randomly distributed pores can be envisioned to be a 'component' of specimens exhibiting EA.

Last but not least, it was shown in ref. (89) that, at very long diffusion times and for very long cylinders, there is a different regime that one must be aware of. Under such conditions, the quadratic term of the signal may have an angular dependence resembling the $\cos(2\psi)$-type dependence because of the CSA effects as discussed above. Surprisingly though, a similar angular dependence emerges in the quadratic term. As spheres are not predicted to yield such angular dependence in the quadratic term of the Taylor series, it can again be attributed to CSA.

Theory of radial d-PFG

So far, we have described the theory for d-PFG experiments with fixed gradient strength when the angle between the two gradients is varied. In 2007, Özarslan and Basser (65) considered the case of multiple-PFG acquisitions with constant gradient orientation, and when the magnitude of the gradients was varied concomitantly. This is the same type of experiment that is typically performed to observe diffraction-like features in s-PFG MR acquisitions (27). However, it was shown in ref. (65) that the diffraction-like features are significantly different in multiple-PFG acquisitions with an even number of gradient pulse pairs. The most important difference is that the signal, rather than rebounding from the horizontal axis, crosses it and acquires negative values. The first zero-crossing occurs at half the q value at which the s-PFG signal minimum occurs. The most important implication of zero-crossing is its robustness to the heterogeneity in the sample. For example, when a population of compartments with different sizes is considered, the signal minimum in s-PFG acquisitions is predicted to disappear quickly. However, because of the cancellations of the positive and negative signals in polydisperse specimens, the zero-crossing is not lost in d-PFG experiments (65). A similar situation occurs in the

presence of orientational dispersion (61). As shown theoretically in ref. (61), the zero-crossing is retained even when the pores are oriented along completely random directions.

After presenting the proof-of-concept for Mitra's limiting cases outlined above, in ref. (65), the authors provided simulations for different numbers of diffusion gradient pulse pairs and different levels of polydispersity. It was shown that, when an odd number of pulse pairs was employed, the robustness to heterogeneity was lost. The effects of variations in the experimental parameters were demonstrated using the matrix formulation (31,92) of the multiple propagator approach that employs the discretization of an arbitrary gradient waveform (91), as mentioned above.

A generalized method for a unified theory

Although the important contributions by Mitra (68) and Cheng and Cory (69) provided the framework and essential ideas for the characterization of restricted diffusion, the assumptions regarding the experimental parameters make it difficult to employ these techniques in real life problems. The main difficulty is that the conditions listed above relate the experimental parameters to geometric quantities – the same quantities one is trying to extract from the data. As such, these quantities cannot be known *a priori*, making it difficult to design an experiment that is guaranteed to be valid for the particular specimen. Moreover, the heterogeneity within the specimen (e.g. pore size distribution) may make it impossible to fulfill all of these conditions for all pores within the specimen. In image acquisitions, the pore dimensions are expected to vary from voxel to voxel – a desirable situation to create image contrast. Therefore, the simplifying assumptions listed above will most likely be violated in some voxels and not in others, leading to an ambiguity in the observed contrast.

The theory based on the analytical evaluation of the quadratic term of the MR signal attenuation provided in ref. (89) enabled the generalization of Mitra's main finding to experiments with arbitrary timing parameters. The only remaining condition, namely the low-q requirement, was overcome in ref. (93) by acquiring data at several small q values and fitting the data at a particular angle to a function of the form:

$$E(q, \psi) \approx 1 - u^2(\psi)q^2 + C(\psi)q^4 \qquad [3]$$

Subsequently, the $u^2(\psi)$ profile was fitted to the theory in ref. (89) to extract the pore dimensions via d-PFG acquisitions with arbitrary timing parameters. This approach is similar to that performed in ref. (69) which used such an expansion for only two values of ψ.

Although the above scheme can be employed to overcome the limitation of the theory regarding the q values, it is typically not desirable because it requires data at several q values. Perhaps more importantly, as demonstrated in ref. (94), the same small q regime may be 'contaminated' by the presence of a freely diffusing component, making the features from restricted diffusion difficult to extract. Clearly, a more general theory that can accommodate all timing parameters together with arbitrary q values would be helpful. Although the matrix product version (31,92) of the multiple propagator approach (91) could be used to that end, the results would be only approximate because of the discretization of the gradient waveform, and accurate estimations would be computationally expensive.

A more feasible theoretical development was recently introduced in ref. (95). The technique employed by the authors involves the generalization of the multiple correlation function (MCF) framework introduced by Grebenkov (96,97). In the MCF framework, a

pseudo-quantum mechanical approach taken by Robertson (98) in the 1960s was refined to quantify the signal for restricted diffusion in well-defined pore shapes. The MCF approach, in its original form, provided exact expressions for piecewise constant gradient waveforms, and approximate results for others, as long as the gradient orientation was held constant throughout the pulse sequence.

This assumption of the MCF framework made it impossible to utilize it for general d-PFG acquisitions where the angle between the two gradients was varied. By employing relatively sophisticated concepts, such as operator algebra and the Wigner–Eckart theorem (99), the necessary generalization that extended the framework to completely arbitrary gradient waveforms was provided (95). The resulting technique can be used to characterize the microstructural features from radial as well as angular d-PFG, hence unifying the two approaches. It should be noted that, similar to that in ref. (89), this unified framework makes it possible to acquire data by varying the timing parameters, such as gradient durations, diffusion periods and mixing times as well. Moreover, the extension in ref. (95) is useful not only in angular d-PFG acquisitions, but also in quantifying the effects of imaging gradients in arbitrary MR acquisitions, as gradients in all three directions have to be applied in three-dimensional k-space imaging. Therefore, by accounting for the effects of imaging gradients, the theory in ref. (95) is expected to yield accurate estimations of the microstructural features, even in multiple-PFG image acquisitions with completely arbitrary parameters.

To summarize, the recent theoretical advances presented the following important features that pertain to obtaining new microstructural information.

1. In the high-q regime, when restricted diffusion is considered in monodisperse pores and d-PFG is conducted in the restricted direction, the theory predicts zero-crossings of the signal decay, which have an extraordinary sensitivity to variations in the experimental parameters, such as the mixing time and diffusion times. Moreover, it has been proposed that, although diffusion–diffraction troughs in s-PFG vanish as a result of size distributions, zero-crossings will persist and report on the lost microstructural information, offering a theoretical solution to one of the most severe limitations of s-PFG.
2. The angular dependence d-PFG experiment can be used to obtain accurate compartmental dimensions from small compartments, even at low q values and at realistic experimental settings, thus obviating the need to reach high q values in which diffusion–diffraction troughs are observed; all nonidealized experimental parameters, such as finite mixing times, varying diffusion periods, gradient durations and compartment orientation, can be accounted for by using the new analysis scheme.
3. A breadth of novel microstructural information can be extracted even when anisotropic compartments are randomly oriented. The theoretical framework enables the extraction of microscopic anisotropy at $t_m = 0$ ms, even in randomly oriented compartments or even, indeed, in spherical pores (Fig. 3A, E, F), and CSA parameters can be extracted at finite mixing times, offering a new method to characterize randomly oriented locally anisotropic compartments.

This advance in the theory significantly broadens the experimental possibilities for obtaining accurate microstructural

information, especially in those regimes in which s-PFG methods are limited. The novel parameters provided by the theory, which cannot be measured using s-PFG methodologies, are expected to play an important role in characterizing GM and other regions in the brain.

EXPERIMENTAL FINDINGS AND VALIDATION OF THE THEORY ON RESTRICTED DIFFUSION PHANTOMS

The theoretical advances discussed in the above section offer a general framework from which many microstructural features could, in principle, be obtained from d-PFG experiments under realistic experimental conditions. However, the validity of these theoretical predictions, as well as the accuracy and robustness of the method, needs to be experimentally assessed prior to application in biological tissues. In a series of recent studies, phantoms for restricted diffusion have been used to test the new theoretical framework. In such phantoms, microstructural parameters, such as the nominal compartment dimensions, geometry and orientation within the magnet, are well defined; therefore, the 'ground truth' of the phantom is known *a priori*, an important advantage for challenging a new theory. These phantoms, consisting of water-filled microcapillaries, have been extensively studied previously using s-PFG methodology (29,30,36,37), and have proven to be useful in characterizing the effects of various experimental parameters on the signal decay. Notably, when monodisperse microcapillaries are used, diffusion–diffraction minima are observed and microstructural information, such as the size and orientation of the microcapillaries, can be accurately

extracted and compared with the nominal size of the microcapillaries. Full experimental details regarding the construction of these phantoms can be found in refs. (29,30,36,37). Briefly, microcapillaries are filled several days prior to each experiment and are densely packed in a 4-mm glass sleeve. The sleeve is then placed in a 5-mm NMR tube with the principal axis of the microcapillaries along the *z* direction (the direction of the main magnetic field). In each section, a brief description of the phantom used is presented.

Observation of zero-crossings and the effect of experimental parameters

The theory for d-PFG signal decay in coherently placed monodisperse compartments included predictions of zero-crossings of the signal that are analogous to the diffusion–diffraction minima in s-PFG experiments (65). The theoretical study in ref. (65) predicted that, for such an array of compartments, the zero-crossings of the signal would occur in d-PFG experiments at a *q* value equal to half of the location of the diffusion–diffraction troughs in s-PFG experiments. Recently, these zero-crossings have been observed experimentally for the first time, and the influence of various experimental parameters on their location was studied (100).

The diffusion–diffraction patterns arising from the diffusion of water in microcapillaries with a nominal inner diameter (ID) of $25 \pm 1 \ \mu$m in a s-PFG experiment conducted in the *x* direction in the long Δ and short δ limits are shown in Fig. 5A. The diffusion–diffraction minima can be easily discerned. Figure 5B shows the $E(q)$ plot extracted from the data (black squares), together with the theoretical fitting to the data (black
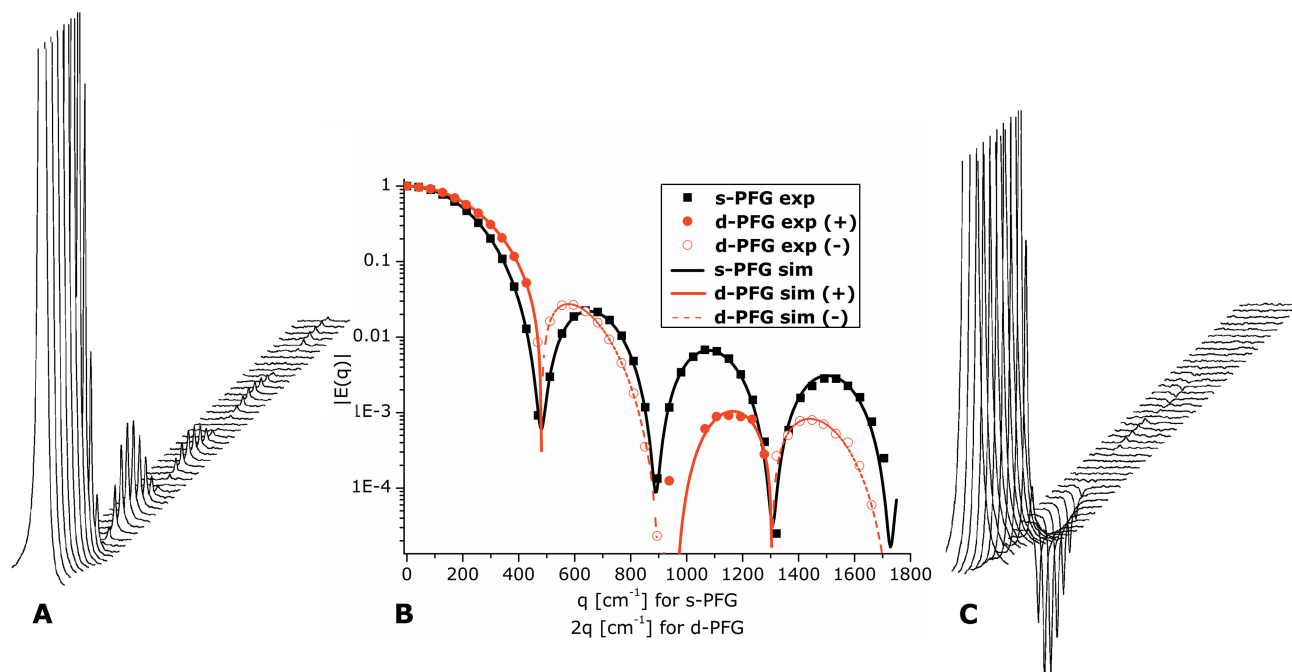

Figure 5. Stackplots and $|E(q)|$ plots of single- (s-PFG) and double-pulsed field gradient (d-PFG) experiments. (A) The stackplot from an s-PFG experiment conducted on microcapillaries with inner diameter (ID) = $25 \pm 1 \ \mu$m with $\Delta/\delta = 150/3$ ms. The diffusion–diffraction minima can be easily observed. (B) Experimental data (symbols) and theoretical fits (lines) for s- and d-PFG experiments (black squares and red circles, respectively). Note that d-PFG negative experimental data and negative theoretical fits are plotted as absolute values (open red circles and broken red line, respectively); therefore, the zero-crossings are manifested as diffusion–diffraction troughs. The data of d-PFG are plotted against 2q to enable easy comparison with s-PFG. (C) The stackplot of a d-PFG experiment conducted on the same microcapillaries with $\Delta_1 = \Delta_2/\delta_1 = \delta_2 = \delta_3 = 150/3$ ms and with $t_m = 0$ ms. Note the actual zero-crossings of the signal, after which the phase of the signal is inverted with respect to the initial phase.

full lines). The diffusion–diffraction troughs occur at $q = 468$, 895 and 1320 cm^{-1}, respectively (data are shown only up to $q = 1800$ cm^{-1} to enable easy comparison with d-PFG results). It should be noted that the size can be either extracted directly from the diffusion–diffraction troughs, yielding sizes of 26.0, 27.3 and 27.7 μm, respectively, or from fitting the data to the theory above, yielding a size of 25.63 ± 0.03 μm. The accuracy of the extracted size from diffusion–diffraction minima is limited by the resolution in the q axis and, for small compartments, by the diffusion during the gradient pulse (violation of the SGP approximation). However, the theoretical framework can account for these effects and the size extracted from the fit to the theory is in excellent agreement with the nominal size.

The signal decay from a corresponding d-PGSE$_{xx}$ experiment is shown in Fig. 5C. Here, the zero-crossing of the signal is apparent. It should be noted that, after the zero-crossing, the signal is in fact negative (i.e. the peak is inverted relative to its initial phase). Figure 5B shows the $|E(q)|$ plot that was extracted from the experiment. The positive experimental points are plotted as red filled symbols, whereas the absolute values of the negative experimental points are plotted as red open symbols (Fig. 5B). The theoretical fitting to the signal is plotted as full lines, with the positive values plotted as red full lines and the absolute values of the negative signal as broken lines. The d-PFG data are plotted against $2q$ to be comparable with s-PFG. It should be noted that the zero-crossings can be observed at $2q = 468$, 895 and 1298 cm^{-1} for the first, second and third zero-crossings, respectively. When the theory presented above is used, a diameter of 25.65 ± 0.03 μm is extracted, in very good agreement with the nominal diameter of 25 ± 1 μm.

In ref. (100), the effect of various experimental parameters on the location of the zero-crossings in different d-PGSE experiments was studied using the d-PGSE sequence shown in Fig. 4A. It was found that prolonging the mixing time shifted the first zero-crossing to higher q values in d-PGSE$_{xx}$ experiments, whereas, for d-PGSE$_{xz}$, the mixing time had no effect whatsoever on the signal decay. Interestingly, the first zero-crossing was found to disappear for orthogonal experiments, because of the loss of motional correlation between free diffusion in the z direction and restricted diffusion in the x direction. The study also showed the equivalence of d-PGSE$_{xz}$ and d-PGSE$_{zx}$, for example, conducted using the same parameters on an ideal phantom. Another interesting finding was that shortening the diffusion periods (concomitantly) resulted in a shift of the zero-crossing towards higher q values (100). The sensitivity of the first zero-crossing to the experimental parameters, demonstrated in this study, implies that care should be taken when extracting microstructural information in such experiments. The experimental findings were consistent with the predictions published previously in ref. (65).

Robustness of zero-crossings in size distribution phantoms

Most realistic specimens commonly have polydisperse or varying compartment dimensions. For example, in neuronal tissues, the axon sizes are distributed around an average diameter which varies for different types of tissue. When specimens are characterized by size distributions, the diffusion–diffraction troughs vanish in s-PFG methodologies (101). However, the theory first presented in ref. (65) predicted that the zero-crossings in d-PFG should persist even in cases of broad size distributions, as long as the diffusion periods are sufficiently long to probe the boundaries of the restricting geometry (102). Hence, restricted

diffusion could be used to infer on microstructural information, even in specimens characterized by broad size distributions.

To test this prediction, size distribution phantoms were prepared: microcapillaries of varying sizes were counted and mixed in a single NMR tube to comprise accurate volumetric ratios. As opposed to realistic size distribution samples, the size distribution in such phantoms is not continuous; nevertheless, it constitutes a platform on which the width and average size distribution are controllable, affording a system in which the 'ground truth' is known. The s- and d-PFG experiments were all conducted in the restricted direction, i.e. the direction perpendicular to the main axis of the microcapillaries.

Figure 6A shows the volumetric ratio of the size distribution phantoms employed in ref. (102), namely SD001, SD002 and SD003. The three specimens can be characterized by an average diameter d_{av} and its standard deviation σ. The phantoms SD001, SD002 and SD003 were constructed such that these parameters were 18.8 ± 1.9, 16.0 ± 4.3 and 14.9 ± 4.6 μm, respectively, yielding $\sigma/r_{av} = 0.10$, 0.27 and 0.31, respectively (where σ is the standard deviation and $r_{av} = d_{av}/2$ is the average radius of the compartment). The theory predicts that, when the sample is characterized by a size distribution in which $\sigma/r_{av} > 0.2$, the diffusion–diffraction troughs vanish in s-PFG.

The experimental signal decay from s-PFG experiments on the size distribution phantoms is shown in Fig. 6B, together with the signal decay from a monodisperse phantom. The monodisperse microcapillaries yielded well-resolved, deep, diffusion–diffraction troughs, with the first minimum observed at $q = 638$ cm^{-1}, corresponding to a compartment size of 19.1 μm. However, the $E(q)$ profile changed dramatically when the measurements were performed on the SD001 phantom. Although SD001 was designed to have only a slight variation of diameters ($\sigma/r_{av} = 0.10$), the signal decay in s-PFG became profoundly more shallow, yielding wider minima which were nevertheless still observable at $q \sim 680$ cm^{-1}. When SD002 and SD003 were used ($\sigma/r_{av} = 0.27$ and 0.31, respectively), the sharp diffusion–diffraction minima were almost completely lost, and it was no longer possible to obtain structural information from the phantom's $E(q)$ profile.

The $E(q)$ plots for the d-PFG experiments performed on these phantoms have a qualitatively different behavior (Fig. 6C) (the data were magnitude calculated and plotted as a function of $2q$ to be comparable with the s-PFG data). Here, the diffusion–diffraction minima are sharp and present for all of the size distribution phantoms used. The location of the first minima for 19 μm (monodisperse), SD001, SD002 and SD003 phantoms are observed at $q = 638$, 680, 808 and 936 cm^{-1}, respectively, corresponding to diameters of 19.1, 17.9, 15.1 and 13.0 μm, respectively. These sizes are in good agreement with the average diameters of the size distribution phantoms, with a slight deviation towards smaller sizes, probably as a result of a slight violation of the SGP approximation.

The real signal decay, without the magnitude calculation, for d-PFG experiments on the monodisperse and polydisperse size distribution phantoms is shown in Fig. 6D. It should be noted that the actual zero-crossing can be observed in these plots. Several features of these plots may be useful in understanding the characteristics of the size distribution, at least qualitatively. The zero-crossing indicates, to a certain extent, the location of the peak of the distribution (although the theory suggests not exactly). Nevertheless, this is new microstructural information that is not accessible by s-PFG (102). Another feature that can be used to infer the width of the distribution is the q value in which a

Copyright © 2010 John Wiley & Sons, Ltd.   View this article online at wileyonlinelibrary.com
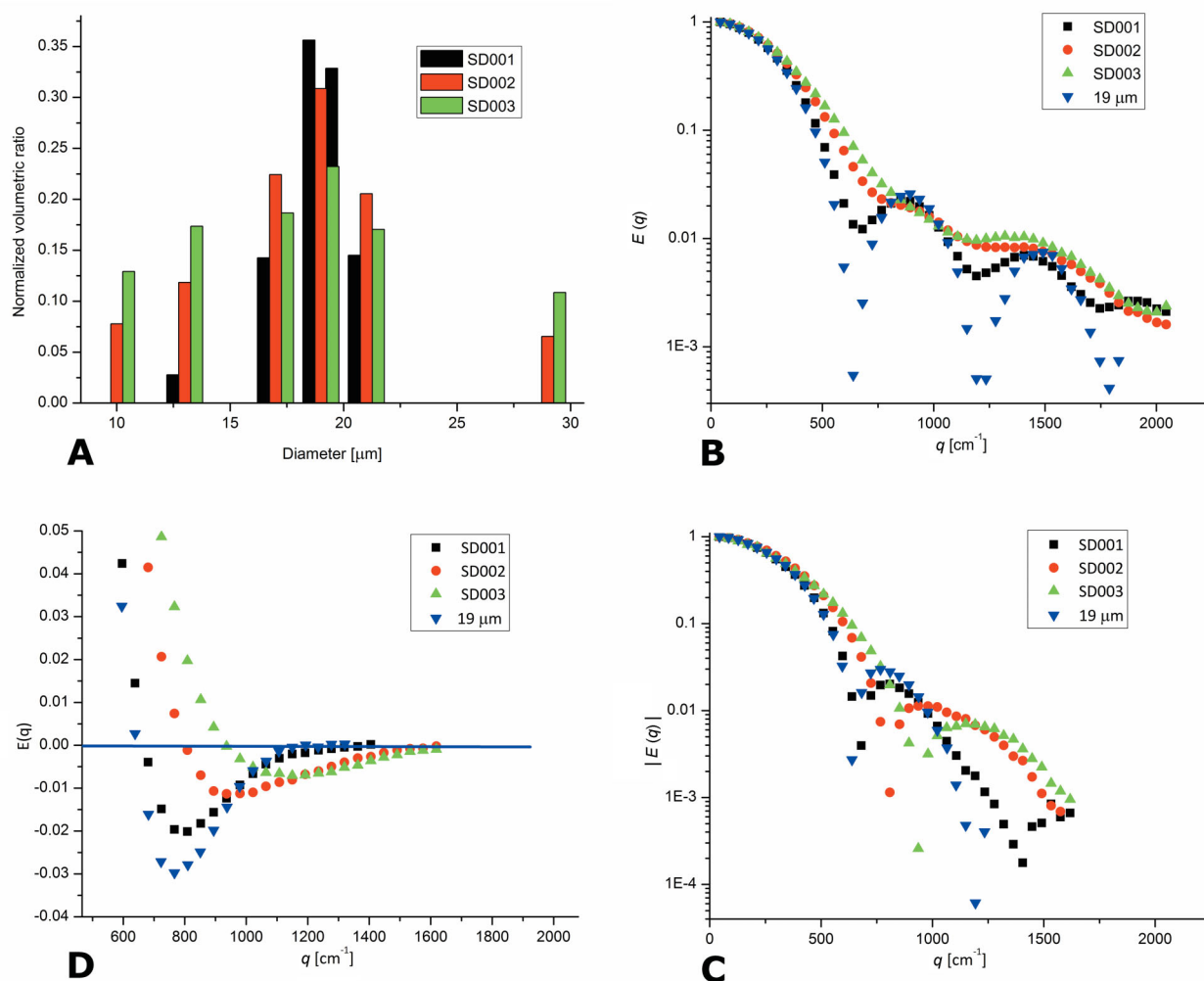
Figure 6. Experiments on size distribution phantoms (102). (A) The volumetric ratio of sizes present in each size distribution phantom. (B) Single-pulsed field gradient (s-PFG) experiments for a monodisperse phantom and for SD001–SD003 shown in (A). s-PFG experiments were carried out with $\Delta/\delta = 150/3$ ms in the long diffusion regime. Note the gradual loss of diffusion–diffraction troughs. (C) The magnitude calculated $|E(q)|$ plots of double-PFG (d-PFG) experiments for the phantoms. Note that $|E(q)|$ plots yield diffraction-like patterns rather than zero-crossings. In these experiments, comparable with the s-PFG experiments, $\Delta_1 = \Delta_2 = 150$ ms and $\delta_1 = \delta_2 = \delta_3 = 3$ ms were used with the sequence shown in Fig. 4B ($t_m = 0$ ms). The data are plotted as a function of $2q$ to enable easy comparison with s-PFG data. Note that the diffusion–diffraction patterns are easily observed; the location of the diffusion–diffraction minima shifts to higher q values between SD001 and SD003. (D) The real (not magnitude calculated) $E(q)$ plots for the d-PFG experiments, shown for a partial range of q values. The signal minimum increases with increasing σ/r_{av} and the rate of return of the signal to zero is slower for increasing values of σ/r_{av}. [Reprinted with permission from (102). Copyright [2010], American Institute of Physics.]

minimum point of the plot is achieved: this point occurs at a higher value of $E(q)$ (i.e. less signal attenuation) with an increasing width of distribution. Finally, the rate of return of the signal to noise levels in the negative part also depends strongly on the width of the distribution (a manifestation of the lack of a second diffusion–diffraction trough in the magnitude calculated plots). The broader the distribution, the slower the signal returns to noise level (102).

In ref. (102), it was also shown, both theoretically and experimentally, that the zero-crossing in specimens characterized by size distribution would be extremely sensitive to the mixing time, and would vanish even when relatively short mixing times are used. To observe zero-crossings in size distribution phantoms, it was demonstrated that the sequence shown in Fig. 4B, in which $t_m = 0$ ms, yields better results. When d-PFG experiments were performed on SD003 with t_m of only 6 ms, the zero-crossings completely vanished, and it was impossible to extract microstructural information from the sample (102). This property

illustrates the utility of having sequences in which $t_m = 0$ ms, especially when zero-crossings are of interest. It should be noted that the zero-crossings are also expected to persist in specimens characterized by randomly oriented but locally anisotropic pores (61); indeed, these findings were very recently validated experimentally (115).

The above study demonstrates that zero-crossings offer new information that is inherently absent from s-PFG MR. It should be noted that it requires a high SNR to detect these zero-crossings in d-PFG experiments, especially for broad distributions, as the signal is expected to remain quite low after the zero-crossings. Moreover, as the size distribution broadens, the location of the zero-crossing is shifted towards higher q values, thus necessitating stronger gradients. For instance, to characterize compartments with $d_{av} = 1.5$ μm and a moderate size distribution (such as axons in WM) using the zero-crossings, one would still need to reach q values of more than $10\,000$ cm^{-1}. Moreover, to fulfill the

SGP condition, very short gradient durations would be necessary. Although small gradient systems can be built that can produce more than 3000 G/cm (57), gradient systems capable of producing ∼5–8 G/cm are found in clinical settings because of safety issues and technological limitations. Therefore, accurate extraction of compartmental dimensions at such weak gradient settings is desirable.

Extracting accurate compartmental dimensions from the angular dependence at low q values

As mentioned in the 'Theory' section, the low-q angular dependence was predicted to yield a signature for restricted diffusion from which significant microstructural parameters could be extracted even at low q values. The full angular profile was first observed in refs. (82,83), employing Mitra's theory to analyze data from a complicated, multicompartmental system, in which the ground truth cannot be easily known; moreover, the difference in the

experimental parameters from those required to use Mitra's simple approximate expression was not explained or accounted for.

The general theoretical framework presented in refs. (61,89,95) allowed the accurate extraction of the compartmental dimensions using arbitrary experimental parameters, not limited to the particular and stringent experimental conditions required to use Mitra's original framework. This new theory was tested in another recent study which was performed on the well-characterized water-filled microcapillaries phantom (93). In this study, both sequences shown in Figs 4A and 4B were used. The angular dependence experiment was performed as follows: G_1 was fixed along the x direction and G_2 was varied in the X–Y plane [see Fig. 4F; for full experimental details, see ref. (93)]. The angular dependence d-PFG experiments were performed for microcapillaries of varying sizes, and for different values of the experimental parameters.

Figure 7A demonstrates the angular dependence observed from microcapillaries with a nominal ID of 5 ± 1 μm using the
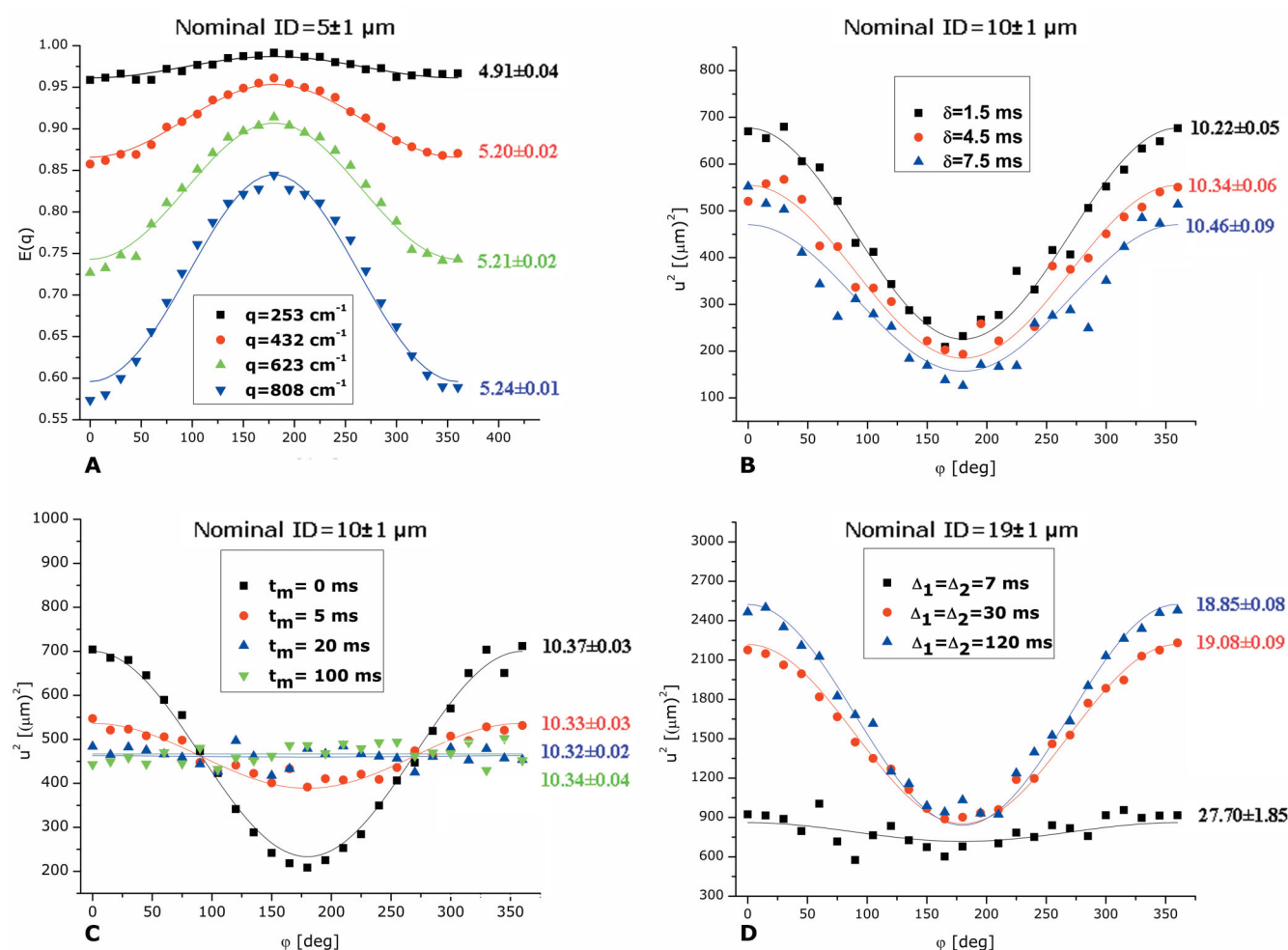

Figure 7. Angular double-pulsed field gradient (d-PFG) experiments conducted on phantoms and the effects of experimental parameters on the signal decay (95,93). (A) Angular d-PFG experiments at different q values for microcapillaries with nominal inner diameter (ID) = 5 ± 1 μm. The experiments were conducted with $\Delta_1 = \Delta_2 = 30$ ms, $\delta_1 = \delta_2 = \delta_3 = 4$ ms and $t_m = 0$ ms. (B) The effect of prolonging the gradient duration in d-PFG experiments. These experiments were conducted on microcapillaries with ID = 10 ± 1 μm. The parameter u^2 is plotted against the angle φ. (C) The effect of prolonging the mixing time (t_m) in d-PFG experiments. These experiments were also conducted on microcapillaries with ID = 10 ± 1 μm and with $\Delta_1 = \Delta_2 = 40$ ms and $\delta_1 = \delta_2 = \delta_3 = 1.5$ ms. The parameter u^2 is plotted against the angle φ. Note the loss of angular dependence at long mixing times when ensemble anisotropy (EA) is present. (D) The effect of prolonging the diffusion periods in d-PFG experiments. These experiments were conducted on microcapillaries with ID = 19 ± 1 μm, $\delta_1 = \delta_2 = \delta_3 = 1.5$ ms and $t_m = 0$ ms. The parameter u^2 is plotted against the angle φ. In all of the plots shown in this figure, the symbols represent experimental data and the full lines represent the theoretical fits to the data. All of the extracted sizes are given in μm. [Reproduced with permission from (93). Copyright [2009], Elsevier.]

sequence shown in Fig. 4B ($t_m = 0$ ms) for different q values, and with Δ long enough to probe the boundaries of the restricting geometry (93). The angular dependence can be clearly observed even at low q values, and follows the predicted bell-shaped function. The compartmental dimension that is extracted for each q value is accurate and in very good agreement with the nominal sizes (the results of the fit can be seen on the graph adjacent to the signal decay). Here, at the lowest q value ($q = 253$ cm^{-1}, comparable with the q value in which DTI is routinely performed), the gradient strength was only 15 G/cm. Moreover, an accurate estimate of the compartmental dimension was extracted with even lower q values [as low as 129 cm^{-1}; data not shown (93)]. For comparison, the compartment size could only have been resolved otherwise using the diffusion–diffraction patterns in s-PFG experiments: the q value which would be needed to observe a diffusion–diffraction dip for 5-μm microcapillaries is 2440 cm^{-1}. However, in order to fulfill the SGP condition, one would have to use very short gradient durations ($\delta \leq 1$ ms), which would necessitate gradient strengths of $|\mathbf{G}| \geq 573$ G/cm, and even then the diffusion–diffraction dip would probably shift to even higher q values because of violation of the SGP condition. The angular dependence, from which accurate sizes were extracted, was observed for microcapillaries with ID $= 9 \pm 1$, 10 ± 1, 19 ± 1, 21 ± 1 and 29 ± 1 μm (data not shown).

An intuitive interpretation for the angular dependence of the signal values can be obtained by examining the signal at $\varphi = 0°$ and $180°$ using the sequence in which $t_m = 0$ ms, as in Fig. 4B or 4D in the long diffusion limit. When $\varphi = 0°$, the total effective gradient strength employed in the sequence is $|\mathbf{G}_{eff}| = |\mathbf{G}_1| + |\mathbf{G}_2|$; however, when $\varphi = 180°$, the middle gradient is absent – therefore, the effective gradient strength is half the size of that employed in $\varphi = 0°$. Effectively, the diffusion period is now doubled, although in the long diffusion limit this is not significant. As the effective gradient is cut in half for $\varphi = 180°$, a reduced signal attenuation or higher $E(q)$ value is obtained (but only for restricted diffusion).

The effects of varying different experimental parameters on the angular dependence were studied in ref. (93). To suppress higher order terms, a combination of four q values (the highest satisfying the $2\pi qa \sim 1$ condition) was used, and the parameter u^2 was plotted against φ. The parameter u^2, whose dimensions are [length]^2, as implied by eqn (3), is analogous to the rmsd of the diffusing moiety in s-PFG.

Figures 7B and 7C show both the experimental results and simulations of the parameter u^2 plotted as a function of φ for microcapillaries with an ID of 10 ± 1 μm with varying gradient durations and mixing times. It should be noted that the u^2 plots show an inverted bell-shaped function when the signal is plotted as a function of φ: this is tantamount to the normal bell-shaped function when $E(\varphi)$ is plotted. Figure 7B shows that, even when the gradient duration is prolonged and the SGP condition is violated, the angular dependence is still observed. The fitting of the experimental results to the theory yielded extremely accurate compartmental dimensions, even when the SGP condition was violated. Figure 7C shows how the angular profile is affected when the mixing time is prolonged; notably, at $t_m > 0$, the angular dependence is significantly diminished, and eventually the angular dependence is completely flat. The fitting to the theory again yielded excellent agreement with the nominal size, even with finite t_m (93), where the angular dependence was less pronounced. It should be noted that, when t_m is prolonged, the

microscopic anisotropy is in fact suppressed, or 'decoupled', from the CSA and EA effects. In the experiment, performed as shown in Fig. 4F, the angular experiment was carried out in the plane normal to the main axis of the microcapillaries; therefore, the molecules probe a circular cross-section and, in such an experiment, CSA is effectively zero (a circle is not anisotropic). This is the reason for the disappearance of the angular dependence at long t_m which leads to a flat angular profile. It should be noted that, in cases of randomly oriented cylinders, or when the experiment is not performed in the plane perpendicular to the main axis of coherently packed cylinders, the CSA effects are predicted to take over at long mixing times, when the microscopic anisotropy effects have been suppressed (61). Experiments on such controlled systems are underway and will be reported in due course, with initial results showing the modulated $E(\psi)$ curves that are expected for CSA.

Figure 7D shows the u^2 plots as a function of concomitantly increasing diffusion times in microcapillaries with ID $= 19 \pm 1$ μm. As expected, the angular dependence almost disappears for very short values of Δ, as the microscopic anisotropy is then sampled only by a small fraction of the diffusing species. In this case, a value of 27.70 ± 1.85 μm is obtained from the fitting of the signal decay, inconsistent with the nominal compartment size. However, prolonging the diffusion period results in the expected angular dependence and the accurate compartmental dimensions can be extracted. It should be noted that, in ref. (93), an inverted angular dependence was also shown for freely diffusing molecules in a nonrestricted isotropic environment for the special case of $\delta \sim \Delta_1 = \Delta_2$ (for the sequence shown in Fig. 4B); there, the inverted angular dependence arises from diffusion during the superposed gradients. In another study, the angular dependence was also shown to persist in size distributions (102).

These studies demonstrate that the compartmental dimensions can be accurately obtained even for very small, biologically relevant sizes. It was demonstrated that the angular dependence is most pronounced when the mixing time is zero, the gradient durations are short and the diffusion periods are sufficiently long to probe the boundaries of the restricting compartment. The angular dependence also becomes more pronounced with increasing q values (95). Importantly, it was shown that the theoretical framework could account for the variation in any experimental parameter, and, as long as the diffusion periods are sufficiently long to probe the boundaries, accurate compartment sizes can be obtained for any combination of experimental parameters.

d-PFG in bicompartmental phantoms

The phantoms used in the previous sections were constructed to produce restricted diffusion. However, many systems consist of bi- or multiple compartments, in which different diffusion modes coexist. One of the most prevalent situations is when free and restricted diffusion coexist. For instance, porous media that are immersed in a solvent constitute a system in which diffusion is restricted within the compartments, but may be free elsewhere. This scenario can also pertain to cell suspensions (restricted within the cells, free in the medium outside) or emulsions (restricted within the emulsion, free outside). In biological applications, the contribution of water from CSF to a voxel that contains WM or even intra- and extracellular water can also be regarded as a system in which the two diffusion modes can coexist. Moreover, crossing fibers, which are exactly

Copyright © 2010 John Wiley & Sons, Ltd.

perpendicular to one another, constitute a multicompartmental system. It would therefore be instructive to study a phantom which represents the scenario presented above, and to study what microstructural features could be obtained in such cases.

To study the signal decay in both s- and d-PFG experiments when restricted and free diffusion coexist, a bicompartmental phantom was constructed (Fig. 8A) [for full details, see (94)]. Briefly, the bicompartmental phantom consists of microcapillaries in which restricted diffusion occurs (termed slow diffusion compartment, SDC), which are placed in a 5-mm NMR tube, which is, in turn, placed inside an 8-mm NMR tube filled with a fixed quantity of H_2O in D_2O (forming the fast diffusion compartment, FDC). The two compartments were completely isolated from each other (i.e. with no exchange), and the FDC was doped with $CuSO_4$ to compensate for relaxation effects (Fig. 8A)

(94). The advantage of using such a phantom is that the ground truth still remains well characterized, namely the orientation of the compartments in the SDC as well as their size is known, and the diffusion coefficient of the water in the FDC is also well known. Therefore, this phantom can be used to investigate the effect of superposing restricted and free diffusion on the signal decay, and to test the theoretical framework in terms of what microstructural information can still be obtained.

In a bicompartmental phantom, it is instructive to first consider two major determinants on the signal decay in s-PFG experiments, namely the effect of the diffusion time and the effect of increasing the ratio of V_{FDC}/V_{SDC}, where V_i is the volume of water in each compartment. The effect of prolonging the diffusion time is shown in Fig. 8B for a bicompartmental phantom. At very short diffusion times, such as $\Delta = 4$ and 10 ms,
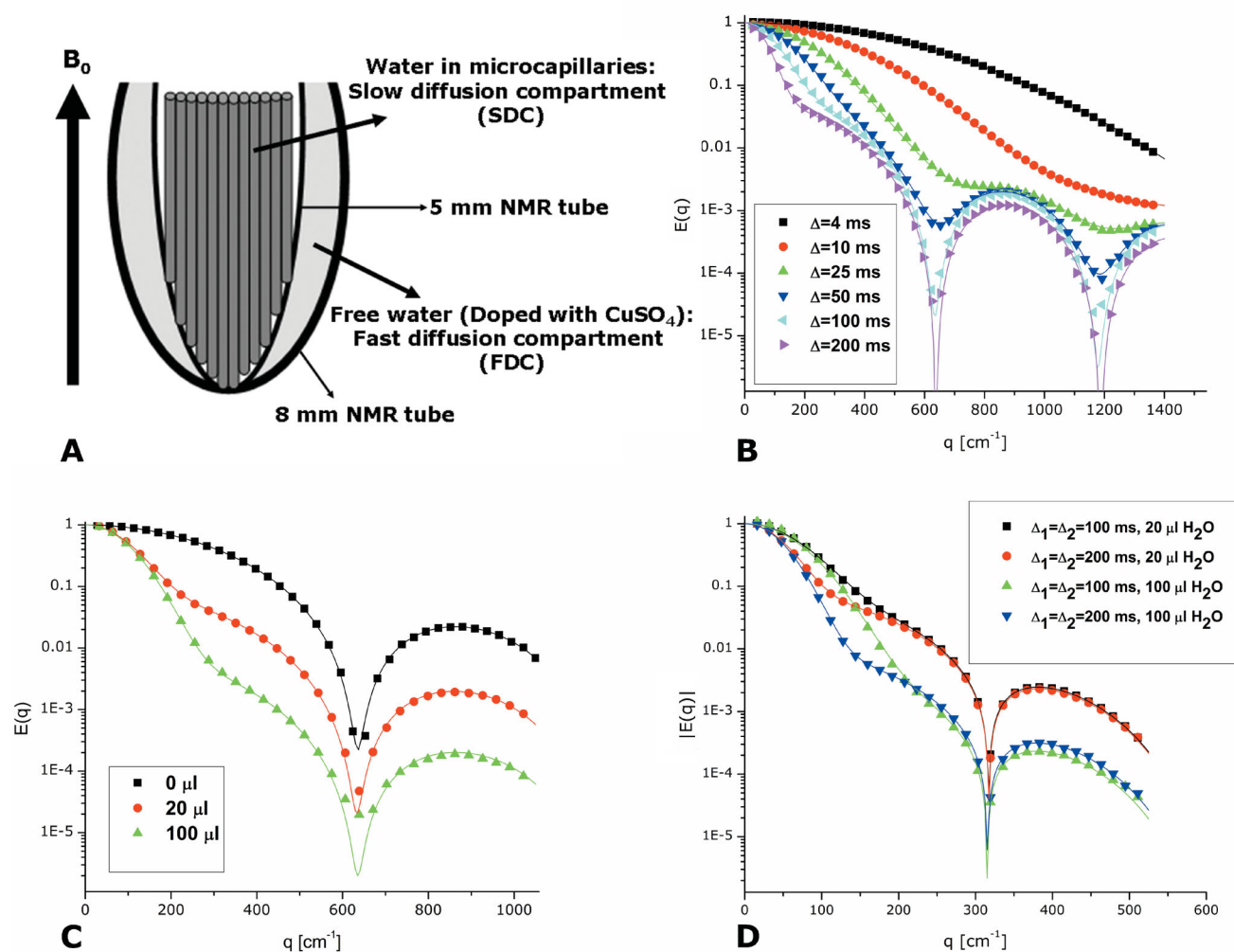

Figure 8. Single- (s-PFG) and double-pulsed field gradient (d-PFG) experiments in the bicompartmental phantom (94). (A) Diagram of the bicompartmental phantom. Microcapillaries are inserted into a 5-mm NMR tube, which is then inserted into an 8-mm NMR tube filled with known quantities of H_2O in D_2O. Note that the water diffusing freely in the fast diffusion compartment (FDC) is completely separated from the microcapillaries (no exchange). The microcapillaries serve as the slow diffusion compartment (SDC), in which restricted diffusion occurs. (B) The s-PFG $E(q)$ plots for varying values of Δ. Note that, in the high-q regime, the diffusion–diffraction minima can be gradually observed. At low q values, the signal attenuation resembles free diffusion. The experiments were performed on microcapillaries with inner diameter (ID) $= 19 \pm 1$ μm and with $\delta = 2$ ms. (C) $|E(q)|$ plots for increasing amounts of water in the FDC. The experiments were performed on microcapillaries with ID $= 19 \pm 1$ μm and with $\Delta/\delta = 100/2$ ms. (D) $|E(q)|$ plots for d-PFG experiments at two different values of diffusion period and for two different amounts of water in the FDC. The same signal trends were observed as in s-PFG experiments. In all of the plots shown in this figure, the symbols represent experimental data and the full lines represent the theoretical fits to the data. Note that the zero-crossings are manifested as diffusion–diffraction troughs in these magnitude calculated $|E(q)|$ plots. [Reproduced with permission from (94). Copyright [2009], Elsevier.]

which are not sufficient to probe the boundaries of the 19 ± 1-μm microcapillaries in the SDC, a free diffusion profile is observed. Prolonging the diffusion time reveals two regimes of diffusion in the signal decay profile. At high q values, diffusion–diffraction troughs first appear, and, when the long diffusion limit is reached ($\Delta = 100$ ms in this case), the signal remains the same for longer Δ. However, at the lower q values, the signal is continuously attenuating with increasing Δ, thereby exhibiting a free profile. There is excellent agreement between the theoretical curves fitted to the theory, and, for $\Delta > 25$ ms, an accurate compartment size could be extracted for the microcapillaries in the SDC (94).

Figure 8C shows the dependence of the signal decay on the amount of water in the FDC, with the amount of water in the SDC remaining constant. Here, the experiment was performed with Δ sufficiently long to probe the boundaries of the restricting compartment. Notably, the diffusion–diffraction trough remains in the same location, but the signal at the lower q values shows a significant attenuation when the amount of water in the FDC is increased. Moreover, the q value in which the transition from free to restricted diffusion occurs is observed at higher q values, probably as the larger amount of free water generates sufficient SNR to be detected even at somewhat higher q values. From these findings, the utility of employing relatively high q values and long diffusion periods is apparent: the free diffusion at low q values simply masks the restricted diffusion, and therefore the microstructural information that can be obtained therefrom is impaired. In ref. (94), it was shown that microstructural information can be retrieved at higher q values for a phantom of crossing microcapillaries, which exhibits a precise bicompartmental behavior; at low q values, as are customary from DTI, the free diffusion indeed masks the restricted compartment, affording only information regarding the free diffusion; at higher q values, diffusion–diffraction minima are present, enabling the extraction of the size and direction of restriction.

Figure 8D shows a d-PFG$_{xx}$ experiment conducted on the bicompartmental phantom with two different diffusion periods and for two different amounts of H_2O in the FDC. The same signal trends as observed for s-PFG were also observed for the d-PFG experiments. The zero-crossings (manifested as a diffusion–diffraction dip in Fig. 8D as a result of the magnitude calculation) appear at the same q value for both $\Delta_1 = \Delta_2 = 100$ and 200 ms (both sufficiently long to fully probe the boundaries of the restricting compartment); however, the signal at the low q values continuously attenuates when Δ is prolonged, exhibiting free diffusion. When the volume fraction of FDC is increased, the q value in which the transition from free to restricted diffusion is observed is shifted to higher q values (Fig. 8D).

Angular dependence in the bicompartmental phantom

As mentioned in the section above, the signal arising from the SDC, which is often desirable for extracting microstructural information, is masked by the signal from the FDC at low q values. In ref. (94), the effect of superposing two diffusion modes on the angular dependence was also addressed. The angular d-PFG experiment shown in Fig. 4F, i.e. where $\mathbf{G_1}$ is fixed along the x axis and $\mathbf{G_2}$ is varied in the X–Y plane (under the long diffusion period condition), was performed in the bicompartmental phantom at different q values and with Δ long enough to probe the boundaries of the restricting compartment within the SDC using the sequence shown in Fig. 4B ($t_m = 0$ ms). Figure 9A shows the

$E(q)$ plot for two different diffusion periods for $\theta = 90°$ and $\varphi = 0°$ (i.e. the d-PFG$_{xx}$ experiment), and the q values for which the angular experiments were performed. The angular profiles obtained revealed two distinct behaviors: at very low q values ($q < 129$ cm^{-1}), the angular dependence was flat (Fig. 9B), and the microstructural information of the compartments was lost; however, at somewhat higher q values, the full angular profile, resembling a bell-shaped function, was retained (Fig. 9C), from which accurate compartmental dimensions were extracted (94). It should be noted that, when only the SDC exists, i.e. without free water, the angular dependence is observed even at the lowest q values, such as those depicted in Fig. 9B. Figure 9D shows the actual NMR signals from the experiment for three q values, from which the robustness of the results is apparent. It should be noted that, in these experiments, although the volume fraction of free water was relatively large, the angular dependence could be observed using weak gradients ($G = 15$ G/cm) and accurate microstructural information could be obtained. In addition, the angular dependence could be observed at even lower q values when the diffusion periods were prolonged (94), in which case the free diffusion is further attenuated and no longer masks the restricted component, thus providing a means to probe microstructural information at low q values, even when the specimen has a significant free diffusion compartment.

Comparing s-PFG and d-PFG experiments

An interesting phenomenon occurs when the signal decay from s-PFG is compared with the signal decay of d-PFG in the bicompartmental phantom. In refs. (65,100), it was shown that, when only a single compartment exists in which restricted diffusion occurs, the location of the zero-crossings in d-PFG occurs at half the q value relative to the location of the diffusion–diffraction troughs in s-PFG. Therefore, by plotting the signal decay in d-PFG as a function of $2q$, s-PFG and d-PFG signal decays are comparable.

In the bicompartmental phantom, plotting the signal decay of d-PFG as a function of $2q$ indeed yields zero-crossings in the same location as in s-PFG (Fig. 10A; d-PFG data are magnitude calculated to reveal the diffraction-like patterns); however, in this case, the signal at low q values, which exhibits free diffusion, is not comparable. However, when the signal decay of d-PFG is plotted against $2^{1/2}q$, the signal in the free regime is comparable between the two methodologies, but the locations of the diffusion–diffraction minima are not (Fig. 10B). This peculiarity arises from the different scaling laws governing the signal decay in d-PFG for the different diffusion modes (94) as expected from the theory (95). Therefore, care should be exercised when comparing the microstructural information when different modes of diffusion are present within the same sample.

d-PFG MRI

Although d-PFG NMR provides powerful new parameters and features with which to characterize *ex vivo* biological specimen and other materials, a *desideratum* would be to produce maps or images of computed quantities *in vivo* to aid in the characterization of microstructural and architectural features of heterogeneous, anisotropic and optically turbid biological tissue, such as brain GM and WM. d-PFG MRI (combining d-PFG NMR with MRI) offers the potential to produce such quantitative maps.
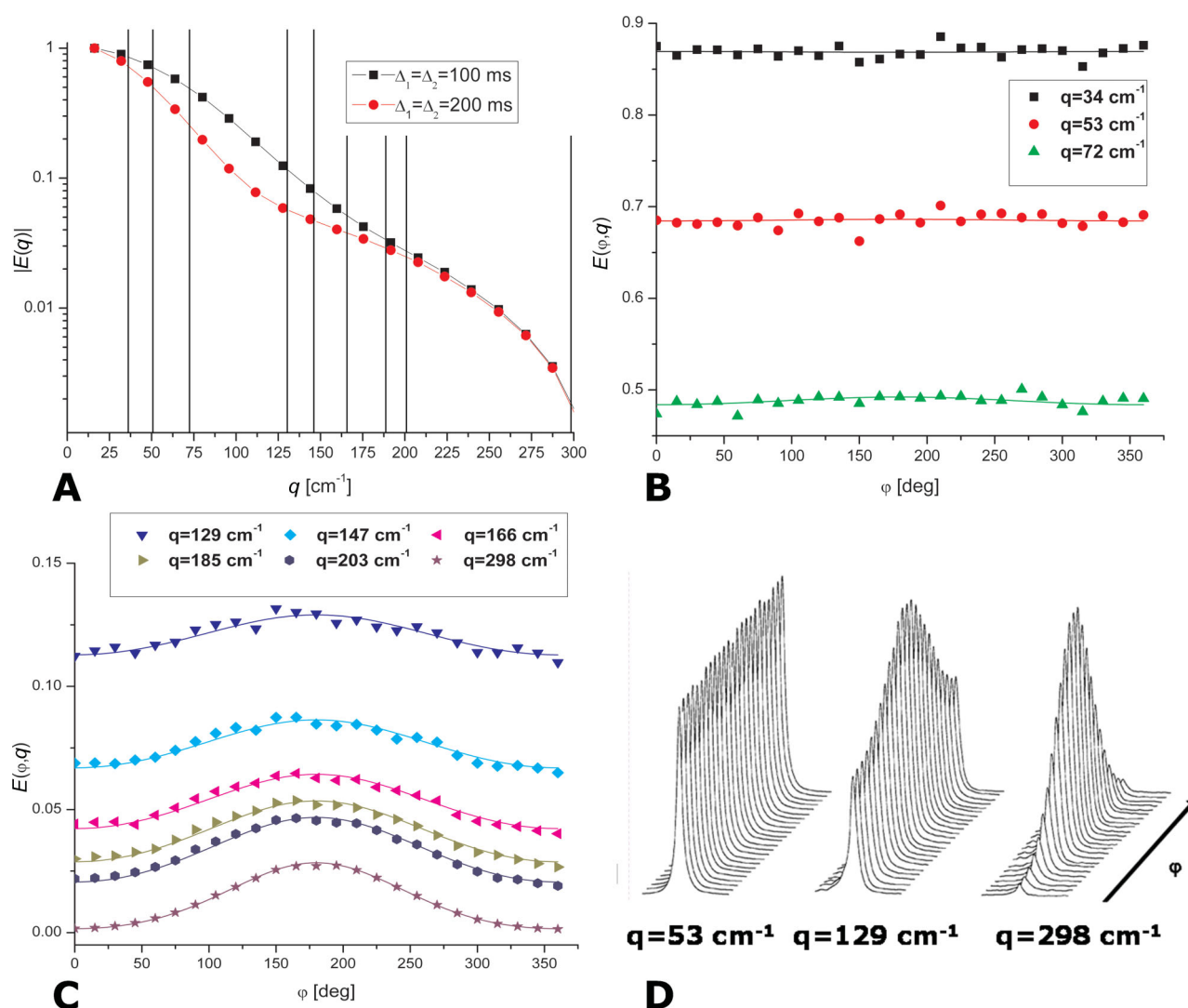
Figure 9. Angular double-pulsed field gradient (d-PFG) experiments in the bicompartmental phantom (94). In this case, the bicompartmental phantom consisted of microcapillaries with inner diameter (ID) $= 19 \pm 1$ μm as the slow diffusion compartment (SDC) and 20 μL of water in the fast diffusion compartment (FDC). (A) The d-PGSE $|E(q)|$ plot for $\varphi = 0°$, i.e. both gradients are in the x direction, perpendicular to the main axis of the microcapillaries. The diffusion times in this experiment were $\Delta_1 = \Delta_2 = 100$ or 200 ms (black squares and red circles, respectively), and $t_m = 0$ ms. The vertical black lines represent the q values for which the angular profile is presented in (B) and (C). (B) The signal intensity plotted against φ for three q values between 34 and 72 cm^{-1}. (C) The signal intensity plotted against φ for q values between 129 and 298 cm^{-1}. The full curves in (A–C) represent the theoretical fits of the experimental data. (D) Raw data for three selected q values of the signal intensity plotted against φ. In all of the plots shown in this figure, the symbols represent experimental data and the full lines represent the theoretical fits to the data. [Reproduced with permission from (94). Copyright [2009], Elsevier.]

The potential of d-PFG MRI is that its improved sensitivity and selectivity to fine microstructural details and features would enable discrimination among different tissue types and architectural motifs that presently are not detectable or discernible using conventional s-PFG MRI methods. These include DTI, all high angular resolution diffusion imaging methods, such as Q-Ball MRI (103), all higher order tensor methods (104,105), composite hindered and restricted model of diffusion (106–108), diffusion orientation transform (109) and diffusion spectrum imaging (110,111). Specifically, this new microstructural information would enable us to segment, classify and cluster different tissues within an imaging volume on the basis of features of the axon diameter distribution, or quantities such as the cell density, cell shape, extracellular volume fraction, etc. This is extremely important information from a biological standpoint, as well as in

following normal and abnormal development, degeneration, disease and aging processes.

In principle, by analogy with diffusion-weighted MRI, it is possible to embed a d-PFG NMR sequence within a conventional MRI sequence to achieve d-PFG MRI (Fig. 11A). Because of a number of experimental difficulties and theoretical complexities (e.g. the proliferation of 'cross-terms' between and among imaging and diffusion gradients, the creation of multiple echoes), it is prudent to separate the d-PFG NMR block and the MRI block in the sequence, effectively using the d-PFG NMR sequence as a 'filter' for the subsequent MRI block which provides spatial localization. This approach was first demonstrated by Komlosh et al. (112).

For the detection of locally anisotropic voxels in pig spinal cord (72), long-τ_m d-PFG NMR sequences were concatenated to an MRI
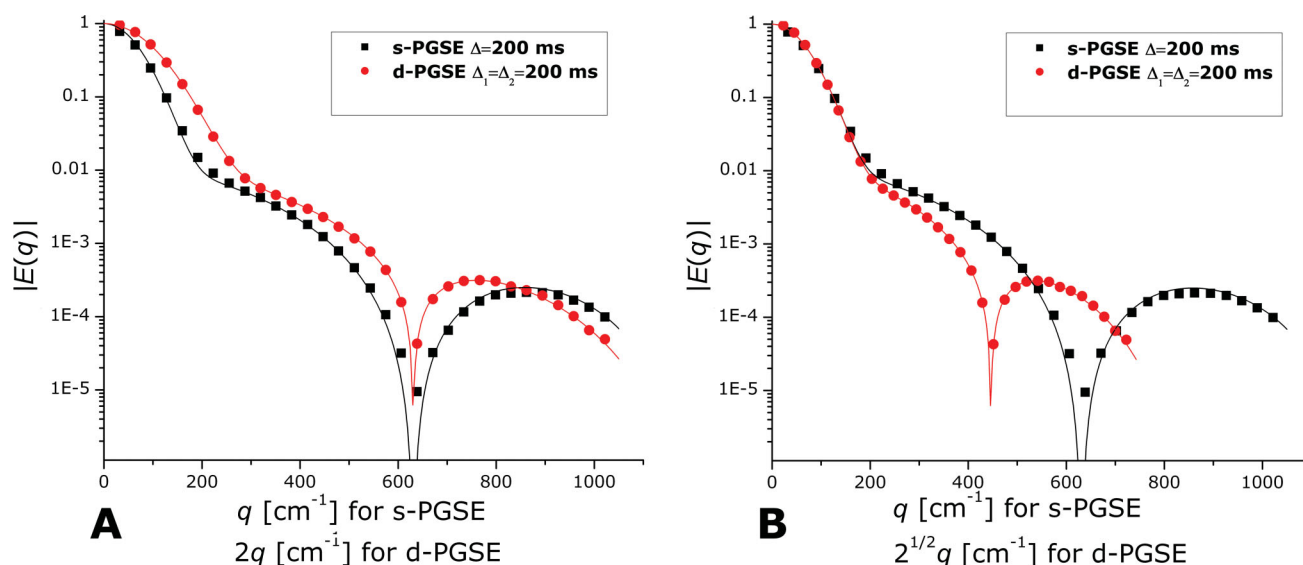
Figure 10. Comparison between single- (s-PFG) and double-pulsed field gradient (d-PFG) signal decays at the different q regimes (94). The bicompartmental phantom consisted of microcapillaries with inner diameter (ID) = 19 ± 1 μm as the slow diffusion compartment (SDC) and 100 μL of water in the fast diffusion compartment (FDC). (A) The s-PGSE data are plotted against q (black squares) and the d-PGSE data are plotted against $2q$ (red circles). (B) The s-PGSE data are plotted against q (black squares) and the d-PGSE data are plotted against $2^{1/2}q$ (red circles). The full lines represent the theoretical curves fitted to the data. Note that the zero-crossings are manifested as diffusion–diffraction troughs in these magnitude calculated $|E(q)|$ plots. [Reproduced with permission from (94). Copyright [2009], Elsevier.]

block to form a d-PFG-filtered MRI sequence (Fig. 11B). This sequence starts with the d-PFG block in which hard RF pulses are applied to form the echo at the point at which the imaging block is applied. The use of hard pulses reduces artifacts resulting from RF inhomogeneity when using shaped pulses. The disadvantage of a d-PFG-filtered MRI sequence is that it prolongs the experiment duration, resulting in a loss of signal due to T_2 relaxation, which can generally be compensated for by using a stimulated echo sequence instead of the spin echo sequence. Although the proof-of-principle was demonstrated on a 'GM' phantom (71), the robustness of the imaging sequence has been shown recently on a phantom consisting of arrays of micro-capillaries, where quantitative size maps could be generated (113). The new theoretical framework used in this study incorporated and modeled the effect of all cross-terms between

diffusion and imaging gradients, as well as the 'fat gradient pulses' which can result in additional diffusion attenuation (113).

Other groups began to develop d-PFG MRI sequences as well. Under the terminology of double-wave-vector imaging, Koch and Finsterbusch conducted an angular d-PFG MRI experiment with finite t_m in three specimens – acrylate beads, radish and excised pig spinal cord (82) – and in human corticospinal tract (83). In these studies, the angle between the q vectors applied in the two PGSE blocks was systematically varied within a d-PFG MRI sequence. Koch and Finsterbusch (82) used an expansion of Mitra's theory, assuming a bicompartmental model in which free (Gaussian) and restricted diffusion are superimposed for all three specimens, including the pig spinal cord. The extracted compartment sizes in the three specimens (82), and in a fiber of corticospinal tract tissue (83), were reported, and the sizes were
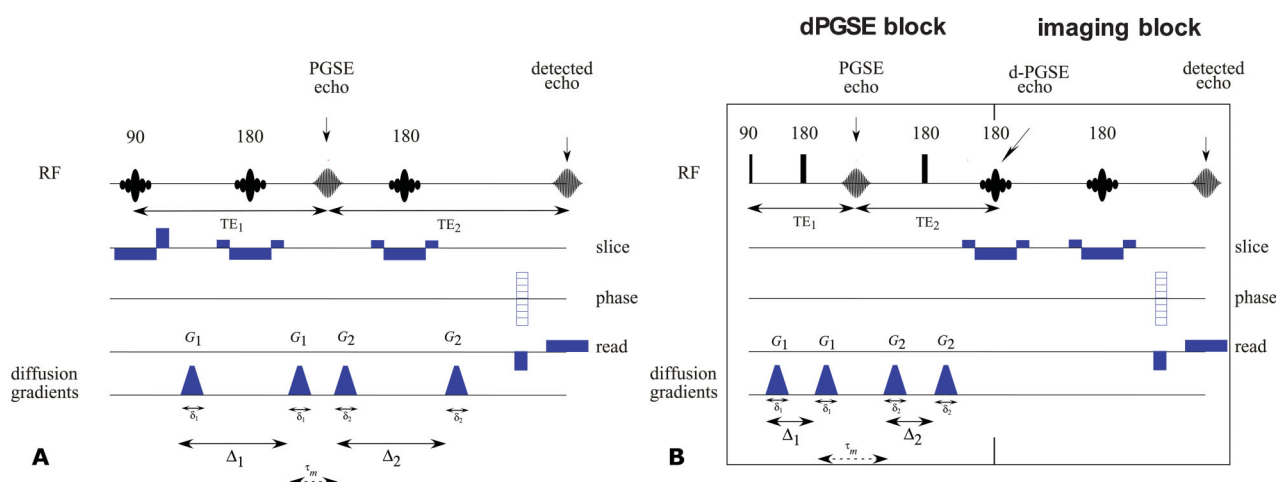

Figure 11. Double-pulsed field gradient (d-PFG) MRI sequences. (A) d-PFG MRI sequence in which the imaging gradients are embedded within the sequence. (B) d-PFG-filtered MRI sequence in which d-PFG is concatenated prior to an imaging block.
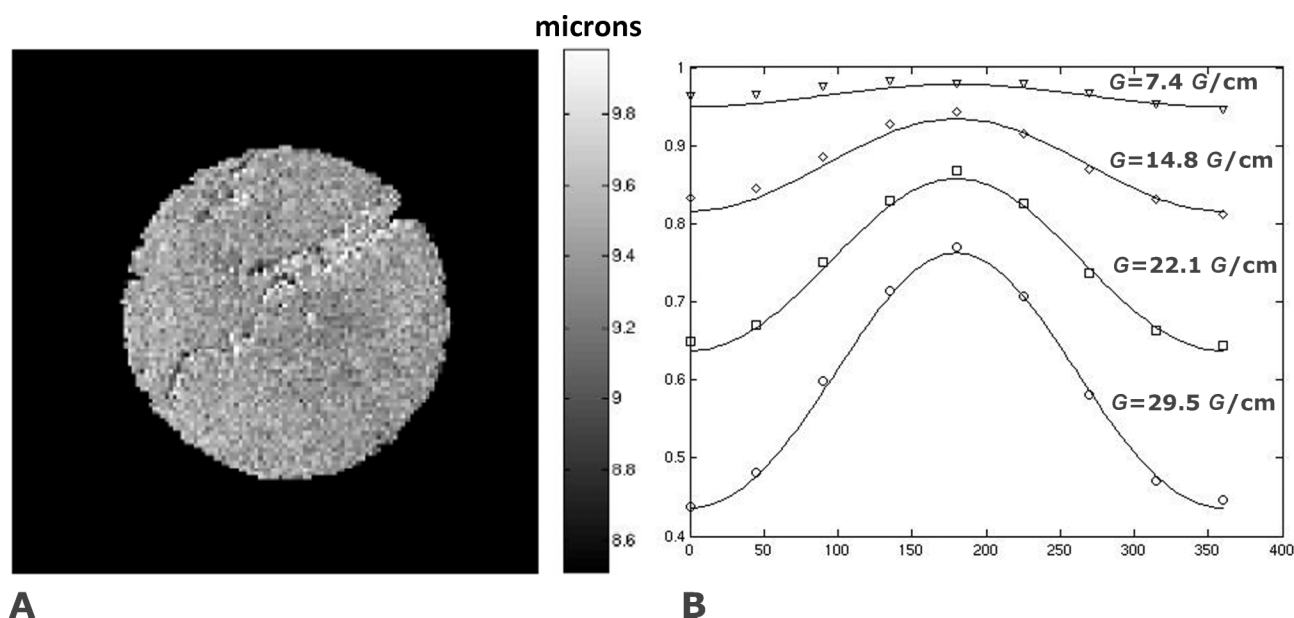
Figure 12. Double-pulsed field gradient (d-PFG) MRI of a glass capillary array (GCA) phantom with inner diameter (ID) = 9.4 ± 0.2 μm (114). (A) A size map obtained from a pixel-by-pixel fit of the angular dependence to the theoretical curves. The scale bar is in μm. (B) The experimental points (symbols) and theoretical curves (full lines) from a region of interest comprising the whole specimen.

on the expected order of magnitude, although no experimental evidence was presented to validate the MR findings. In subsequent studies, Monte Carlo simulations were used to assess the effect of deviation from Mitra's limiting conditions, where it was found that such deviations significantly altered the extracted sizes (84,87). The findings were consistent with the effect of varying experimental parameters in s-PFG (30): when δ is prolonged, the extracted size is smaller (as a result of violation of the SGP approximation), and a smaller size will also be obtained when Δ is too short to probe the boundaries of the restricting compartment. Another finding was that the higher the q value at which d-PFG is performed, the larger the deviation of the extracted size, owing to the deviation from Mitra's condition ($2\pi qR < 1$), and that, in smaller compartments (such as axons in the CNS), the deviation would be most significant.

In ref. (84), the angular dependence was observed when a d-PFG MRI sequence with $t_m = 0$ ms was used to investigate compartment sizes in excised rat spinal cord, and it was shown that the apparent size varies with the diffusion periods as expected from the Monte Carlo simulations. Further Monte Carlo simulations were used to study the signal decay in multiple-PFG (86) and in various tensor approaches (85,88), all utilizing expansions of Mitra's theory to analyze the signal decay.

These studies accentuate the need to use the new theoretical framework (61,95) for the extraction of accurate compartmental dimensions when nonidealized experimental parameters are employed. In ref. (93), it was shown that the use of Mitra's theory leads to substantial deviations from the nominal size, even in water-filled microcapillaries in d-PFG spectroscopy, whereas accurate sizes are extracted from the new theoretical framework. These deviations are most likely to become even more significant when imaging sequences are used in complex tissue, such as neuronal tissue, characterized by multiple diffusion modes, size and orientation distributions, and exchange. Therefore, experimental validation of the MRI results and the theoretical framework, which should take into account 'fat' gradient pulses and cross-terms between and among diffusion and imaging gradients, is imperative.

A new theoretical framework that incorporated and modeled the effect of all cross-terms between diffusion and imaging gradients, as well as 'fat gradient pulses' that can result in additional diffusion attenuation, was used to analyze d-PFG MRI data from the glass capillary array (GCA) phantom mentioned above (114). In this study, a d-PGSE-filtered MRI sequence (Fig. 11B) was applied to the GCA phantom. Specifically, an angular dependence experiment was performed in which $\mathbf{G_1}$ was fixed along the x direction and $\mathbf{G_2}$ was varied in the X–Y plane, as shown in Fig. 4F. The experiment was performed using gradient strengths of 7.4, 14.8, 22.1 and 29.5 G/cm and $t_m = 0$ ms. A map corresponding to the compartment size generated from the experimental angular dependence is shown in Fig. 12A. Importantly, the expected dimensions (e.g. 9 μm) could be extracted from the pore diameter distribution map (Fig. 12A), corresponding well to the nominal size. Figure 12B demonstrates the angular dependence observed from the GCA phantom, and demonstrates the robustness of the angular dependence at the different q values. This study validated the method and theory on a well-characterized MRI phantom, giving us more confidence that this imaging method can now be applied to more complex systems, such as biological specimens.

Looking forward to future clinical applications of d-PFG MRI, it will be necessary to use soft RF pulses and to incorporate the d-PFG block within the imaging block because of clinical instrument limitations. In this configuration, in which imaging and diffusion gradients are not separated in different blocks, cross-terms arise. Therefore, a model, such as the new theoretical framework (95), which takes into account all gradients used in the sequence, must be applied to analyze the signal decay.

SUMMARY AND ASSESSMENT OF FUTURE PROSPECTS

d-PFG methodology holds great promise as a probe for gleaning important new microstructural information in complex speci-

mens (such as neuronal tissues) owing to the significant experimental and theoretical advances presented in this review. The first step, validation of the new theoretical framework of restricted diffusion in d-PFG, has been achieved using MR phantoms in which the ground truth is known *a priori*. Indeed, the experimental results and theoretical predictions are in excellent agreement. Most importantly, d-PFG MR yields accurate compartmental dimensions at low q values, exhibits zero-crossings when size distributions are present, and provides unique microstructural information in randomly oriented compartments that are macroscopically isotropic, even when these are polydisperse. Bipolar versions of d-PFG sequences may be important for the study of inhomogeneous specimens. Importantly, the general theoretical framework can account for variations of all experimental parameters in the d-PFG NMR or MRI sequences; therefore, it provides an extremely accurate means for extracting novel microstructural information.

d-PFG methodology may become extremely useful in at least two significant biomedical applications: In WM, it may characterize axon sizes and size distributions at low, clinically achievable q values; in GM, it may provide important information regarding the size and shape of randomly oriented cells and cell processes. Indeed very recent findings show that even when anisotropic compartments are completely randomly oriented, variants of the angular d-PFG methodology yield novel microstructural information on local pore shape and size (115). Furthermore, preliminary results of angular d-PFG in yeast cells imply that accurate cellular sizes can be obtained even in realistic biological specimens (116). Moreover, d-PFG can even be used to 'filter' unwanted components or compartments, and therefore may play an important role in basic research, for example, to help make assignments of water in different intra- and extracellular compartments.

d-PFG MRI, although in its infancy, may well provide new forms of contrast that may have clinical relevance. For example, the mapping of axonal sizes or size distributions using clinically achievable magnetic field gradients may become an important tool for the characterization of WM development and disease. New microstructural features may be even more important in the characterization of GM, in which conventional s-PFG MRI methods provide limited information. Further studies are needed to evaluate the applicability of d-PFG as a probe for microstructural information in tissues, and new modeling and analysis schemes may be needed to describe diffusion in more complex media. It should be noted that, although this review focuses on biologically oriented applications, the principles demonstrated are general and should be valid in a variety of other applications, such as in MR of porous media, for example to characterize emulsions or rocks.

Acknowledgements

REFERENCES

1. Hahn EL. Spin echoes. Phys. Rev. 1950; 80: 580–594.
2. Carr HY, Purcell EM. Effects of diffusion on free precession in nuclear magnetic resonance experiments. Phys. Rev. 1954; 94: 630–638.
3. Stejskal EO, Tanner JE. Spin diffusion measurements – spin echoes in presence of a time-dependent field gradient. J. Chem. Phys. 1965; 42: 288–292.
4. Price WS. Pulsed-field gradient nuclear magnetic resonance as a tool for studying translational diffusion. 1. Basic theory. Concepts Magn. Reson. 1997; 9: 299–336.
5. Waldeck AR, Kuchel PW, Lennon AJ, Chapman BE. NMR diffusion measurements to characterise membrane transport and solute binding. Prog. Nucl. Magn. Reson. Spectrosc. 1997; 30: 39–68.
6. Johnson CS. Diffusion ordered nuclear magnetic resonance spectroscopy: principles and applications. Prog. Nucl. Magn. Reson. Spectrosc. 1999; 34: 203–256.
7. Le Bihan D, Mangin JF, Poupon C, Clark CA, Pappata S, Molko N, Chabriat H. Diffusion tensor imaging: concepts and applications. J. Magn. Reson. Imaging, 2001; 13: 534–546.
8. Basser PJ, Jones DK. Diffusion-tensor MRI: theory, experimental design and data analysis – a technical review. NMR Biomed. 2002; 15: 456–467.
9. Horsfield MA, Jones DK. Applications of diffusion-weighted and diffusion tensor MRI to white matter diseases – a review. NMR Biomed. 2002; 15: 570–577.
10. Cohen Y, Assaf Y. High b-value q-space analyzed diffusion-weighted MRS and MRI in neuronal tissues – a technical review. NMR Biomed. 2002; 15: 516–542.
11. Mori S, van Zijl PC. Fiber tracking: principles and strategies – a technical review. NMR Biomed. 2002; 15: 468–480.
12. Beaulieu C. The basis of anisotropic water diffusion in the nervous system – a technical review. NMR Biomed. 2002; 15: 435–455.
13. Sen PN. Diffusion and tissue microstructure. J. Phys. Condens. Matter, 2004; 16: S5213–S5220.
14. Cohen Y, Avram L, Frish L. Diffusion NMR spectroscopy in supramolecular and combinatorial chemistry: an old parameter – new insights. Angew. Chem. Int. Ed. 2005; 44: 520–554.
15. Stark DD, Bradley WG. *Magnetic Resonance Imaging*, 3rd edn. Mosby: St. Louis, MO, 1999.
16. Johansen-Berg H, Behrens TEJ. *Diffusion MRI: from Quantitative Measurement to In-vivo Neuroanatomy*. Academic Press, Elsevier: London, 2009.
17. Moseley ME, Cohen Y, Kucharczyk J, Mintorovitch J, Asgari HS, Wendland MF, Tsuruda J, Norman D. Diffusion-weighted MR imaging of anisotropic water diffusion in cat central-nervous-system. Radiology, 1990; 176: 439–445.
18. Moseley ME, Cohen Y, Mintorovitch J, Chileuitt L, Shimizu H, Kucharczyk J, Wendland MF, Weinstein PR. Early detection of regional cerebral-ischemia in cats – comparison of diffusion-weighted and T2-weighted MRI and spectroscopy. Magn. Reson. Med. 1990; 14: 330–346.
19. Basser PJ, Mattiello J, Lebihan D. Estimation of the effective self-diffusion tensor from the NMR spin-echo. J. Magn. Reson. B, 1994; 103: 247–254.
20. Callaghan PT, Codd SL, Seymour JD. Spatial coherence phenomena arising from translational spin motion in gradient spin echo experiments. Concepts Magn. Reson. 1999; 11: 181–202.
21. Sen PN. Time-dependent diffusion coefficient as a probe of geometry. Concepts Magn. Reson. A, 2004; 23A: 1–21.
22. Sotak CH. The role of diffusion tensor imaging in the evaluation of ischemic brain injury – a review. NMR Biomed. 2002; 15: 561–569.
23. Kuchel PW, Durrant CJ, Chapman BE, Jarrett PS, Regan DG. Evidence of red cell alignment in the magnetic field of an NMR spectrometer based on the diffusion tensor of water. J. Magn. Reson. 2000; 145: 291–301.
24. Niendorf T, Dijkhuizen RM, Norris DG, Campagne MV, Nicolay K. Biexponential diffusion attenuation in various states of brain tissue: implications for diffusion-weighted imaging. Magn. Reson. Med. 1996; 36: 847–857.
25. Assaf Y, Cohen Y. Non-mono-exponential attenuation of water and N-acetyl aspartate signals due to diffusion in brain tissue. J. Magn. Reson. 1998; 131: 69–85.
26. Assaf Y, Ben-Bashat D, Chapman J, Peled S, Biton IE, Kafri M, Segev Y, Hendler T, Korczyn AD, Graif M, Cohen Y. High b-value q-space analyzed diffusion-weighted MRI: application to multiple sclerosis. Magn. Reson. Med. 2002; 47: 115–126.
27. Callaghan PT, Coy A, Macgowan D, Packer KJ, Zelaya FO. Diffraction-like effects in NMR diffusion studies of fluids in porous solids. Nature, 1991; 351: 467–469.

28. Callaghan PT. Pulsed-gradient spin-echo NMR for planar, cylindrical, and spherical pores under conditions of wall relaxation. J. Magn. Reson. A, 1995; 113: 53–59.

29. Avram L, Assaf Y, Cohen Y. The effect of rotational angle and experimental parameters on the diffraction patterns and micro-structural information obtained from q-space diffusion NMR: implication for diffusion in white matter fibers. J. Magn. Reson. 2004; 169: 30–38.

30. Avram L, Özarslan E, Assaf Y, Bar-Shir A, Cohen Y, Basser PJ. Three-dimensional water diffusion in impermeable cylindrical tubes: theory versus experiments. NMR Biomed. 2008; 21: 888–898.

31. Codd SL, Callaghan PT. Spin echo analysis of restricted diffusion under generalized gradient waveforms: planar, cylindrical, and spherical pores with wall relaxivity. J. Magn. Reson. 1999; 137: 358–372.

32. Coy A, Callaghan PT. Pulsed gradient spin-echo NMR diffusive diffraction experiments on water surrounding close-packed polymer spheres. J. Colloid Interface Sci. 1994; 168: 373–379.

33. Coy A, Callaghan PT. Pulsed gradient spin-echo nuclear-magnetic-resonance for molecules diffusing between partially reflecting rectangular barriers. J. Chem. Phys. 1994; 101: 4599–4609.

34. Topgaard D, Malmborg C, Soderman O. Restricted self-diffusion of water in a highly concentrated W/O emulsion studied using modu-lated gradient spin-echo NMR. J. Magn. Reson. 2002; 156: 195–201.

35. Kuntz JF, Trausch G, Palmas P, Mutzenhardt P, Canet D. Diffusive diffraction phenomenon in a porous polymer material observed by NMR using radio-frequency field gradients. J. Chem. Phys. 2007; 126: 134904.

36. Bar-Shir A, Avram L, Özarslan E, Basser PJ, Cohen Y. The effect of the diffusion time and pulse gradient duration ratio on the diffraction pattern and the structural information estimated from q-space diffusion MR: experiments and simulations. J. Magn. Reson. 2008; 194: 230–236.

37. Bar-Shir A, Cohen Y. Crossing fibers, diffractions and nonhomoge-neous magnetic field: correction of artifacts by bipolar gradient pulses. Magn. Reson. Imaging, 2008; 26: 801–808.

38. Kuchel PW, Coy A, Stilbs P. NMR 'diffusion–diffraction' of water revealing alignment of erythrocytes in a magnetic field and their dimensions and membrane transport characteristics. Magn. Reson. Med. 1997; 37: 637–643.

39. Torres AM, Michniewicz RJ, Chapman BE, Young GAR, Kuchel PW. Characterisation of erythrocyte shapes and sizes by NMR diffusion–diffraction of water: correlations with electron micrographs. Magn. Reson. Imaging, 1998; 16: 423–434.

40. Torres AM, Taurins AT, Regan DG, Chapman BE, Kuchel PW. Assign-ment of coherence features in NMR q-space plots to particular diffusion modes in erythrocyte suspensions. J. Magn. Reson. 1999; 138: 135–143.

41. Regan DG, Kuchel PW. Simulations of molecular diffusion in lattices of cells: insights for NMR of red blood cells. Biophys. J. 2002; 83: 161–171.

42. Regan DG, Kuchel PW. Simulations of NMR-detected diffusion in suspensions of red cells: the 'signatures' in q-space plots of various lattice arrangements. Eur. Biophys. J. Biophys. Lett. 2003; 31: 563–574.

43. Regan DG, Kuchel PW. NMR studies of diffusion-coherence phenom-ena in red cell suspensions: current status. Isr. J. Chem. 2003; 43: 45–54.

44. Regan DG, Kuchel PW. Simulations of NMR-detected diffusion in suspensions of red cells: the effects of variation in membrane permeability and observation time. Eur. Biophys. J. Biophys. Lett. 2003; 32: 671–675.

45. Pages G, Szekely D, Kuchel PW. Erythrocyte-shape evolution recorded with fast-measurement NMR diffusion–diffraction. J. Magn. Reson. Imaging, 2008; 28: 1409–1416.

46. Larkin TJ, Kuchel PW. Erythrocyte orientational and cell volume effects on NMR q-space analysis: simulations of restricted diffusion. Eur. Biophys. J. Biophys. Lett. 2009; 39: 139–148.

47. Cory DG, Garroway AN. Measurement of translational displacement probabilities by NMR – an indicator of compartmentation. Magn. Reson. Med. 1990; 14: 435–444.

48. Kuchel PW, Eykyn TR, Regan DG. Measurement of compartment size in q-space experiments: Fourier transform of the second derivative. Magn. Reson. Med. 2004; 52: 907–912.

49. Assaf Y, Mayk A, Cohen Y. Displacement imaging of spinal cord using q-space diffusion-weighted MRI. Magn. Reson. Med. 2000; 44: 713–722.

50. Bar-Shir A, Cohen Y. High b-value q-space diffusion MRS of nerves: structural information and comparison with histological evidence. NMR Biomed. 2008; 21: 165–174.

51. Bar-Shir A, Cohen Y. The effect of the rotational angle on MR diffusion indices in nerves: is the rms displacement of the slow-diffusing component a good measure of fiber orientation? J. Magn. Reson. 2008; 190: 33–42.

52. Assaf Y, Cohen Y. Inferring microstructural information of white matter from diffusion MRI. In Diffusion MRI, Johansen-Berg H, Beherns TEJ (eds). Academic Press, 2009; 127–146.

53. Bar-Shir A, Duncan ID, Cohen Y. QSI and DTI of excised brains of the myelin-deficient rat. Neuroimage, 2009; 48: 109–116.

54. Biton IE, Duncan ID, Cohen Y. q-space diffusion of myelin-deficient spinal cords. Magn. Reson. Med. 2007; 58: 993–1000.

55. Farrell JA, Smith SA, Gordon-Lipkin EM, Reich DS, Calabresi PA, van Zijl PC. High b-value q-space diffusion-weighted MRI of the human cervical spinal cord in vivo: feasibility and application to multiple sclerosis. Magn. Reson. Med. 2008; 59: 1079–1089.

56. Mayzel-Oreg O, Assaf Y, Gigi A, Ben-Bashat D, Verchovsky R, Mordo-hovitch M, Graif M, Hendler T, Korczyn A, Cohen Y. High b-value diffusion imaging of dementia: application to vascular dementia and Alzheimer disease. J. Neurol. Sci. 2007; 257: 105–113.

57. Ong HH, Wright AC, Wehrli SL, Souza A, Schwartz ED, Hwang SN, Wehrli FW. Indirect measurement of regional axon diameter in excised mouse spinal cord with q-space imaging: simulation and experimental studies. Neuroimage, 2008; 40: 1619–1632.

58. Assaf Y, Blumenfeld-Katzir T, Yovel Y, Basser PJ. AxCaliber: a method for measuring axon diameter distribution from diffusion MRI. Magn. Reson. Med. 2008; 59: 1347–1354.

59. Barazany D, Basser PJ, Assaf Y. In vivo measurement of axon diameter distribution in the corpus callosum of rat brain. Brain, 2009; 132: 1210–1220.

60. Biton IE, Mayk A, Kidron D, Assaf Y, Cohen Y. Improved detectability of experimental allergic encephalomyelitis in excised swine spinal cords by high b-value q-space DWI. Exp. Neurol. 2005; 195: 437–446.

61. Özarslan E. Compartment shape anisotropy (CSA) revealed by double pulsed field gradient MR. J. Magn. Reson. 2009; 199: 56–67.

62. Pelta MD, Morris GA, Stchedroff MJ, Hammond SJ. A one-shot sequence for high-resolution diffusion-ordered spectroscopy. Magn. Reson. Chem. 2002; 40: S147–S152.

63. Xu JZ, Does MD, Gore JC. Quantitative characterization of tissue microstructure with temporal diffusion spectroscopy. J. Magn. Reson. 2009; 200: 189–197.

64. Khrapitchev AA, Callaghan PT. Double PGSE NMR with stimulated echoes: phase cycles for the selection of desired encoding. J. Magn. Reson. 2001; 152: 259–268.

65. Özarslan E, Basser PJ. MR diffusion–'diffraction' phenomenon in multi-pulse-field-gradient experiments. J. Magn. Reson. 2007; 188: 285–294.

66. Callaghan PT, Godefroy S, Ryland BN. Use of the second dimension in PGSE NMR studies of porous media. Magn. Reson. Imaging, 2003; 21: 243–248.

67. Cory DG, Garroway AN, Miller JB. Applications of spin transport as a probe of local geometry. Polymer Preprints, 1990; 31: 149.

68. Mitra PP. Multiple wave-vector extensions of the NMR pulsed-field-gradient spin-echo diffusion measurement. Phys. Rev. B, 1995; 51: 15074–15078.

69. Cheng Y, Cory DG. Multiple scattering by NMR. J. Am. Chem. Soc. 1999; 121: 7935–7936.

70. Callaghan PT, Komlosh ME. Locally anisotropic motion in a macro-scopically isotropic system: displacement correlations measured using double pulsed gradient spin-echo NMR. Magn. Reson. Chem. 2002; 40: S15–S19.

71. Komlosh ME, Horkay F, Freldlin RZ, Nevo U, Assaf Y, Basser PJ. Detection of microscopic anisotropy in gray matter and in a novel tissue phantom using double pulsed gradient spin echo MR. J. Magn. Reson. 2007; 189: 38–45.

72. Komlosh ME, Lizak MJ, Horkay F, Freidlin RZ, Basser PJ. Observation of microscopic diffusion anisotropy in the spinal cord using double-pulsed gradient spin echo MRI. Magn. Reson. Med. 2008; 59: 803–809.

Copyright © 2010 John Wiley & Sons, Ltd. View this article online at wileyonlinelibrary.com

73. Momot KI, Kuchel PW. PFG NMR diffusion experiments for complex systems. Concepts Magn. Reson. A, 2006; 28A: 249–269.

74. Jerschow A, Muller N. Suppression of convection artifacts in stimulated-echo diffusion experiments. Double-stimulated-echo experiments. J. Magn. Reson. 1997; 125: 372–375.

75. Momot KI, Kuchel PW. Convection-compensating PGSE experiment incorporating excitation-sculpting water suppression (CONVEX). J. Magn. Reson. 2004; 169: 92–101.

76. Seymour JD, Callaghan PT. Generalized approach to NMR analysis of flow and dispersion in porous media. Aiche J. 1997; 43: 2096–2111.

77. Blumich B, Callaghan PT, Damion RA, Han S, Khrapitchev AA, Packer KJ, Stapf S. Two-dimensional NMR of velocity exchange: VEXSY and SERPENT. J. Magn. Reson. 2001; 152: 162–167.

78. Callaghan PT, Khrapitchev AA. Time-dependent velocities in porous media dispersive flow. Magn. Reson. Imaging, 2001; 19: 301–305.

79. Callaghan PT, Furo I. Diffusion–diffusion correlation and exchange as a signature for local order and dynamics. J. Chem. Phys. 2004; 120: 4032–4038.

80. Callaghan PT, Arns CH, Galvosas P, Hunter MW, Qiao Y, Washburn KE. Recent Fourier and Laplace perspectives for multidimensional NMR in porous media. Magn. Reson. Imaging, 2007; 25: 441–444.

81. Galvosas P, Qiao Y, Schonhoff M, Callaghan PT. On the use of 2D correlation and exchange NMR spectroscopy in organic porous materials. Magn. Reson. Imaging, 2007; 25: 497–500.

82. Koch MA, Finsterbusch J. Compartment size estimation with double wave vector diffusion-weighted imaging. Magn. Reson. Med. 2008; 60: 90–101.

83. Koch MA, Finsterbusch J. Double wave vector diffusion weighting imaging in the human corticospinal tract in vivo. Proc. Int. Soc. Magn. Reson. Med. 2008; 16: 764.

84. Weber T, Ziener CH, Kampf T, Herold V, Bauer WR, Jakob PM. Measurement of apparent cell radii using a multiple wave vector diffusion experiment. Magn. Reson. Med. 2009; 61: 1001–1006.

85. Finsterbusch J, Koch MA. A tensor approach to double wave vector diffusion-weighting experiments on restricted diffusion. J. Magn. Reson. 2008; 195: 23–32.

86. Finsterbusch J. Extension of the double-wave-vector diffusion-weighting experiment to multiple concatenations. J. Magn. Reson. 2009; 198: 174–182.

87. Koch MA, Finsterbusch J. Numerical simulation of double-wave vector experiments investigating diffusion in randomly oriented ellipsoidal pores. Magn. Reson. Med. 2009; 62: 247–254.

88. Lawrenz M, Koch MA, Finsterbusch J. A tensor model and measures of microscopic anisotropy for double-wave-vector diffusion-weighting experiments with long mixing times. J. Magn. Reson. 2010; 202: 43–56.

89. Özarslan E, Basser PJ. Microscopic anisotropy revealed by NMR double pulsed field gradient experiments with arbitrary timing parameters. J. Chem. Phys. 2008; 128: 154511.

90. Özarslan E, Nevo U, Basser PJ. Anisotropy induced by macroscopic boundaries: surface-normal mapping using diffusion-weighted imaging. Biophys. J. 2008; 94: 2809–2818.

91. Caprihan A, Wang LZ, Fukushima E. A multiple-narrow-pulse approximation for restricted diffusion in a time-varying field gradient. J. Magn. Reson. A, 1996; 118: 94–102.

92. Callaghan PT. A simple matrix formalism for spin echo analysis of restricted diffusion under generalized gradient waveforms. J. Magn. Reson. 1997; 129: 74–84.

93. Shemesh N, Özarslan E, Basser PJ, Cohen Y. Measuring small compartmental dimensions with low-q angular double-PGSE NMR: the effect of experimental parameters on signal decay. J. Magn. Reson. 2009; 198: 15–23.

94. Shemesh N, Özarslan E, Bar-Shir A, Basser PJ, Cohen Y. Observation of restricted diffusion in the presence of a free diffusion compartment: single- and double-PFG experiments. J. Magn. Reson. 2009; 200: 214–225.

95. Özarslan E, Shemesh N, Basser PJ. A general framework to quantify the effect of restricted diffusion on the NMR signal with applications to double pulsed field gradient NMR experiments. J. Chem. Phys. 2009; 130: 104702.

96. Grebenkov DS. NMR survey of reflected Brownian motion. Rev. Mod. Phys. 2007; 79: 1077–1137.

97. Grebenkov DS. Analytical solution for restricted diffusion in circular and spherical layers under inhomogeneous magnetic fields. J. Chem. Phys. 2008; 128: 134702.

98. Robertson B. Spin-echo decay of spins diffusing in a bounded region. Phys. Rev. 1966; 151: 273–277.

99. Merzbacher E. *Quantum Mechanics*. John Wiley & Sons: New York, 1998.

100. Shemesh N, Cohen Y. The effect of experimental parameters on the signal decay in double-PGSE experiments: negative diffractions and enhancement of structural information. J. Magn. Reson. 2008; 195: 153–161.

101. Price WS, Stilbs P, Soderman O. Determination of pore space shape and size in porous systems using NMR diffusimetry. Beyond the short gradient pulse approximation. J. Magn. Reson. 2003; 160: 139–143.

102. Shemesh N, Özarslan E, Basser PJ, Cohen Y. Detecting diffusion–diffraction patterns in size distribution phantoms using double-pulsed field gradient (d-PFG) NMR: theory and experiment. J. Chem. Phys. 2010; 132: 034703.

103. Tuch DS, Reese TG, Wiegell MR, Wedeen VJ. Diffusion MRI of complex neural architecture. Neuron, 2003; 40: 885–895.

104. Özarslan E, Mareci TH. Generalized diffusion tensor imaging and analytical relationships between diffusion tensor imaging and high angular resolution diffusion imaging. Magn. Reson. Med. 2003; 50: 955–965.

105. Liu CL, Bammer R, Moseley ME. Generalized diffusion tensor imaging (GDTI): a method for characterizing and imaging diffusion anisotropy caused by non-Gaussian diffusion. Isr. J. Chem. 2003; 43: 145–154.

106. Alexander DC. A general framework for experiment design in diffusion MRI and its application in measuring direct tissue-microstructure features. Magn. Reson. Med. 2008; 60: 439–448.

107. Assaf Y, Freidlin RZ, Rohde GK, Basser PJ. New modeling and experimental framework to characterize hindered and restricted water diffusion in brain white matter. Magn. Reson. Med. 2004; 52: 965–978.

108. Assaf Y, Basser PJ. Composite hindered and restricted model of diffusion (CHARMED) MR imaging of the human brain. Neuroimage, 2005; 27: 48–58.

109. Özarslan E, Shepherd TM, Vemuri BC, Blackband SJ, Mareci TH. Resolution of complex tissue microarchitecture using the diffusion orientation transform (DOT). Neuroimage, 2006; 31: 1086–1103.

110. Wedeen VJ, Hagmann P, Tseng WYI, Reese TG, Weisskoff RM. Mapping complex tissue architecture with diffusion spectrum magnetic resonance imaging. Magn. Reson. Med. 2005; 54: 1377–1386.

111. Wedeen VJ, Wang RP, Schmahmann JD, Benner T, Tseng WYI, Dai G, Pandya DN, Hagmann P, D'Arceuil H, de Crespignya AJ. Diffusion spectrum magnetic resonance imaging (DSI) tractography of crossing fibers. Neuroimage 2008; 41: 1267–1277.

112. Komlosh ME, Horkay F, Freidlin RZ, Assaf Y, Basser PJ. Detection of local anisotropy using double-PGSE filtered imaging. *Proceedings of the 47th Experimental Nuclear Magnetic Resonance Conference*. Pacific Grove: CA, USA, 2006; E060077.

113. Komlosh ME, Özarslan E, Lizak MJ, Horkay F, Basser PJ. Pore diameter measured using d-PGSE filtered MRI. *10th International Conference on Magnetic Resonance Microscopy*. West Yellowstone: MT, USA, 2009; P02.

114. Komlosh ME, Özarslan E, Horkay F, Basser PJ. Fiber diameter mapping of a white matter phantom using d-PFG filtered MRI. Proc. Int. Soc. Magn. Reson. Med. 2010; 18: 3399.

115. Shemesh N, Özarslan E, Adiri T, Basser PJ, Cohen Y. Noninvasive bipolar double-pulsed-field-gradient NMR reveals signatures for pore size and shape in polydisperse, randomly oriented, inhomogeneous porous media. J. Chem. Phys. 2010; 133: 044705.

116. Shemesh N, Özarslan E, Adiri T, Basser PJ, Cohen Y. First observation of microscopic anisotropy (μA) and compartment shape anisotropy (CSA) in randomly oriented biological cells. Proc. Int. Soc. Magn. Reson. Med. 2010; 18: 193.